

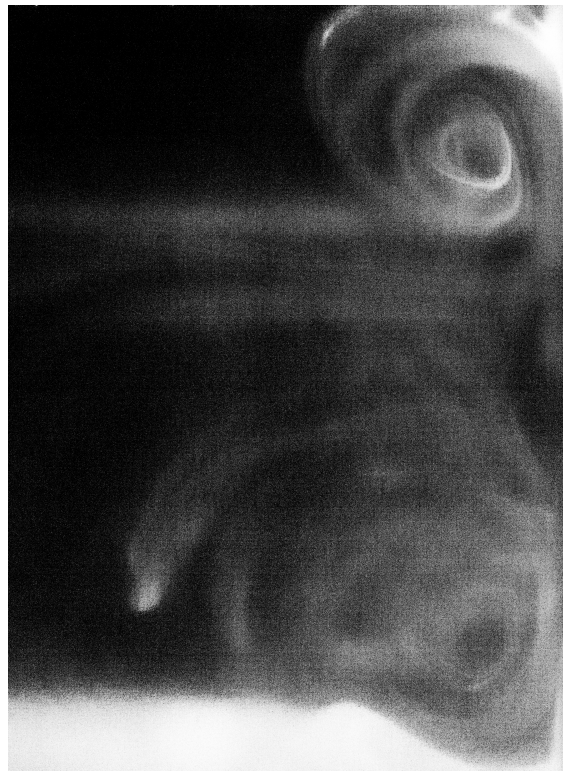
---

# Visualization and Pressure Measurements of the Oscillatory flow in a Jet Pump

---

Bachelor Assignment Advanced Technology

*Frederieke van Dixhoorn*



May 9, 2014

Thermal Engineering Group - University of Twente

BACHELOR COMMITTEE:

Prof. Dr. ir. T.H. van der Meer

Prof. Dr. ir. A. de Boer

J.P. Oosterhuis, MSc

# 1 Abstract

In closed-loop thermoacoustic engines a time-averaged mass flux known as Gedeon streaming can exist [18]. This Gedeon streaming results in a heat leak that causes the efficiency of the engine to decrease. A narrowed, tapered tube section, known as a jet pump, can suppress this time-averaged mass flux. By taking advantage of asymmetry in hydrodynamic end effects a pressure drop can be imposed across the jet pump [18]. In this bachelor's assignment a jet pump is designed with a geometry chosen in order to impose such a pressure drop. For experimentation with this jet pump a test section is introduced within an experimental set-up consisting of a loudspeaker, a cone, and a resonator tube. This experimental set-up is used at the University of Twente for research in thermoacoustics.

Two different sets of experiments are performed with the jet pump section: pressure measurements and flow visualization experiments. The results of the pressure measurements are analyzed and compared with an analytical model as well as a simulated model. The models show a clear match with the experimental results; however, this remains only an initial estimation. To obtain qualitative images of the flow field of the acoustic wave at several instances in time the existing technique of smoke flow visualization [20] is extended and optimized. The main features which are altered are the camera triggering and the method of smoke injection. Various images are captured at a range of pressure amplitudes displaying clear flow patterns. However, the technique of smoke flow visualization remains problematic and a clear image of the flow field of one period of the acoustic wave was not obtained.

# Contents

<b>1</b>	<b>Abstract</b>	<b>2</b>
<b>2</b>	<b>Introduction</b>	<b>4</b>
<b>3</b>	<b>Theory</b>	<b>6</b>
3.1	Jet pump theory . . . . .	6
3.2	Restrictions on the design . . . . .	10
3.3	Jet pump design . . . . .	11
3.4	Simulation of flow field . . . . .	12
<b>4</b>	<b>Experimental set-up</b>	<b>15</b>
4.1	Existing set-up . . . . .	15
4.1.1	Camera . . . . .	16
4.1.2	Laser . . . . .	16
4.1.3	Smoke generator . . . . .	16
4.1.4	Pressure sensors and pressure gauge . . . . .	17
4.2	Pressure measurements . . . . .	18
4.2.1	Comparison of sensors and differential pressure gauge . . . . .	18
4.2.2	Regulation of mean pressure . . . . .	21
4.3	Flow visualization . . . . .	25
4.3.1	Smoke injection . . . . .	25
4.3.2	Camera positioning and triggering . . . . .	27
4.3.3	Laser positioning . . . . .	28
4.3.4	Camera box and smoke box . . . . .	29
4.3.5	High speed camera and laser recommendation . . . . .	29
<b>5</b>	<b>Experiments and results</b>	<b>32</b>
5.1	Pressure measurements . . . . .	32
5.1.1	Time-averaged pressure drop measurements . . . . .	32
5.1.2	Comparison with analytical model and simulations . . . . .	34
5.2	Flow visualization . . . . .	36
5.2.1	Description of observed flow structures . . . . .	36
<b>6</b>	<b>Discussion and Recommendations</b>	<b>41</b>
6.0.2	Pressure measurements . . . . .	41
6.0.3	Flow visualization . . . . .	41
6.0.4	Jet pump design . . . . .	43
<b>7</b>	<b>Conclusion</b>	<b>45</b>
<b>8</b>	<b>Appendix</b>	<b>48</b>
8.1	Preliminary experiments . . . . .	48
8.2	Flow studied per phase at a pressure amplitude of 40 Pa, 60 Pa and 80 Pa . . . . .	51
8.3	Flow studied per phase at a pressure amplitude of 60 Pa with the smoke injected before the jet pump . . . . .	54

## 2 Introduction

As the name suggests, thermoacoustics is the combination of the fields of thermodynamics and acoustics. In 1777 the very first investigations were done on the thermoacoustic effect by Byron Higgins. Higgins performed an experiment in which he showed how the excitation by a single heat source could produce acoustic oscillations [17]. His device was simple, the “Higgins’ singing flame”, and the first qualitative explanation of this thermoacoustic effect only came when Lord Rayleigh said in *The Theory of Sound* [17]:

*If heat be given to air at the moment of greatest condensation (compression) or taken from it at the moment of greatest rarefaction (expansion), the vibration is encouraged.*

The opposite process is also true, and a thermoacoustic engine uses this phenomena. The concept states that an acoustic wave in a channel with a temperature gradient can cause thermal expansion and contraction. When a traveling wave is used in such a thermoacoustic engine the working principle of the engine would be similar to a Stirling cycle [19]. In such a traveling wave thermoacoustic engine a regenerator creates a temperature gradient between a hot heat exchanger and a cold heat exchanger, converting heat to acoustic power. An example of such an engine is shown in Figure 2.1, designed by the Los Alamos group. At the University of Twente, extensive research is being done on thermoacoustic engines.

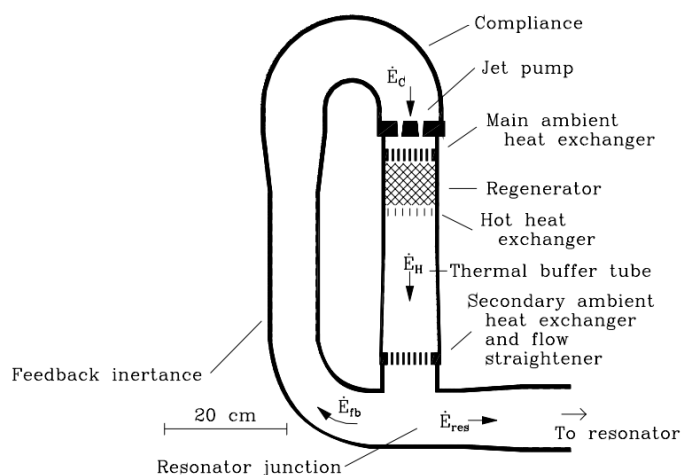


Figure 2.1: Theromoacoustic engine designed by the Los Alamos group [18].

In thermoacoustic systems that contain a closed-loop path, such as the one which is studied, it is possible for a time-averaged mass flux to exist, known as Gedeon streaming [18]. The Gedeon streaming results in a transfer of heat from the hot heat exchanger to the cold heat exchanger. This heat leak leads to a reduced efficiency of the system [18]. The mass flux which can exist in such a thermoacoustic engine as described above is something which is to be avoided. Ideally, a zero time-averaged mass flux is achieved in this system.

In order to achieve a zero time-averaged mass flux a pressure drop must be imposed to balance the existing time-averaged pressure drop across the regenerator in the thermoacoustic set-up, this will be explained in more detail in section 3.1. A method to introduce such a pressure drop is by making use of the asymmetry of hydrodynamic end effects [18]. Energy is dissipated when

flow experiences an abrupt transition from a pipe with a small cross-sectional area to one with a larger cross-sectional area. This dissipation of energy is a result of the jet flow and turbulence which occurs during this process, and is known as “minor loss”. Minor losses in steady flow result in a decrease of flow energy, and in oscillating flow they create time-averaged pressure gradients and dissipate acoustic power [3]. This time-averaged pressure gradient is exactly what is needed to counteract the time-averaged mass flux in the thermoacoustic engine.

A jet pump is a tapered tube section which fulfills this task of creating a time-averaged pressure gradient in oscillatory flows. The fact that the section is tapered is key because otherwise the same minor loss would take place at both ends of the section and there would be no asymmetry in the pressure drop. The asymmetry in the pressure drop is what results in a time-averaged pressure gradient that eventually balances out the existing pressure drop in the thermoacoustic engine and results in a zero mass flux. One of the main goals of this bachelor assignment is to design such a jet pump.

An experimental set-up has been developed in the laboratory of Thermal Engineering at the University of Twente which is used for experimental research in the field of thermoacoustics. The main elements of this set-up are a loudspeaker, a cone and a resonator tube [16]. The loudspeaker produces an acoustic wave in the set-up which is amplified due to the transition in diameter of the cone and is allowed to pass through the resonator tube. Further details on the experimental set-up are provided in section 4.1. One of the main goals of this set-up is to study geometries that cannot be simulated, using numerical models, in a reasonable amount of time and to determine whether these numerical models are able to accurately predict measurements made experimentally. This experimental set-up will be used during this bachelor assignment.

The goals of this bachelor assignment are to extend the existing technique of smoke flow visualization; to design and manufacture a jet pump, to perform pressure measurements with the jet pump, and to perform flow visualization experiments with the jet pump sample. A technique has been developed for flow visualization using smoke flow [20]. However, this needs to be extended to be able to obtain qualitative images of the flow field of the acoustic wave at several instances in time in a more controlled manner.

In chapter 3 a literature study is used to present the theory behind the jet pump and subsequently to design and manufacture one. A description of the existing experimental set-up is given in section 4.1, including a description of the experimental apparatus used. In section 4.2 the method of measuring the pressure over the jet pump using a pressure gauge and digital pressure sensors is compared. In addition to the investigation into the use of a pressure valve to eliminate the mean pressure build up in the set-up. Section 4.3 describes the method of flow visualization and the various elements of this method, including the camera triggering and the smoke injection.

Two main sets of experiments are performed and presented in chapter 5: pressure measurements and flow visualization. The measurement of time-averaged pressure drops is presented in section 5.1, including the comparison of these results with an analytical and simulated model. Flow visualization tests at a range of pressure amplitudes are presented and analyzed in section 5.2. Following the analysis of the results are recommendations for future research and a final conclusion.

# 3 Theory

## 3.1 Jet pump theory

In thermoacoustic systems, with a closed-loop path, a second-order, time-averaged mass flux can exist. This is defined by Equation (3.1), where  $U_{2,0}$  is the second-order time-independent volumetric velocity and  $\dot{W}$  is the time-averaged acoustic power flow [18]. This mass flux results in an undesired convection of heat from the hot heat exchanger to the secondary cold heat exchanger. This convection of heat is an unwanted heat leak of  $\dot{Q}_{leak} = \dot{M}_2 c_p (T_h - T_c)$  where  $c_p$  is the constant-pressure heat capacity of the working fluid [18]. For the optimization of such a thermoacoustic system it is desirable to avoid this heat leak, which can only be done by ensuring that a mass flux of zero is achieved as the other variables will always be nonzero.

$$\dot{M}_2 = \dot{W} + \rho_m U_{2,0} \quad (3.1)$$

The first term on the right hand side of Equation (3.1) is the time-averaged acoustic power flow, defined as the flux in sound energy per unit time. This is nonzero in the thermoacoustic engine which is studied. Thus, in order to ensure that there is no mass flux a  $U_{2,0}$  must be imposed to cancel the first term. A method to impose such a  $U_{2,0}$  is by creating a pressure drop across the regenerator by using the asymmetry of hydrodynamic end effects [18]. The Bernoulli equation (3.2), where  $p$  is the pressure,  $\rho$  the density, and  $u$  the velocity, dictates that in steady, incompressible, laminar flow as the velocity increases the pressure will decrease correspondingly. When this flow is considered to be passing through a pipe with a gradually decreasing cross-sectional area, the mean velocity of the flow will increase due to mass conservation and the pressure will decrease accordingly. Such a decrease in cross-sectional area can thus be used in order to create a specific flow velocity which will lead to zero mass flux.

$$p + \frac{1}{2} \rho u^2 = constant \quad (3.2)$$

Considering a straight pipe with an abrupt decrease in cross-sectional area, the sudden change gives rise to flow separation, vortex shedding, turbulence, and jetting [1]. These are the hydrodynamic end effects referred to earlier. This oscillatory flow which is created by these dissipative processes has as a result that Bernoulli's equation (3.2) is no longer valid. The sudden transition thus leads to an additional pressure drop, compared to the gradual case, which is known as "minor loss". Although referred to as a *minor* loss it is important in the case studied because this pressure drop can lead to a  $U_{2,0}$  which will enforce there to be zero mass flux.

For this reason it is desirable to design an abrupt decrease in cross-sectional area which creates a pressure drop that ensures zero mass flux. Such an abrupt decrease in cross-sectional area can be made in the form of a jet pump. A jet pump is a constriction in a tube which is formed from two transitions in cross-section connected by a conical taper [1]. As is illustrated in Figure 3.1, where the dotted line indicates the rotational symmetry. The abrupt contractions occur as the cross-sectional area where the flow is allowed to pass through decreases from the larger outer tube to either the big or small opening of the jet pump. The expansions occur when the flow travels in the other direction, from the smaller area to the large outer tube.

To study the pressure drop and the discussed phenomena in a jet pump, various pressure measurements and flow visualization experiments will be performed. For these experiments a symmetric jet pump is designed with a geometry that corresponds to that shown in Figure 3.1,

where only the top half is shown. The main dimensions of the jet pump are the big radius ( $R_b$ ), the small radius ( $R_s$ ) and the length of the jet pump ( $L_{JP}$ ). The arc with a radius of curvature  $R_{curv}$  can be described by the four points seen in Figure 3.1:  $A, B, C$  and  $D$ , where  $\alpha$  is the the jet pump cone half-angle. When  $R_{curv} > 0$  the effective small exit radius ( $R_{s,eff}$ ) is used instead of  $R_s$ . The coordinates of the points  $A, C$  and  $D$  with  $B$  being the origin of the local coordinate system  $(x, r)_{JP}$  are:

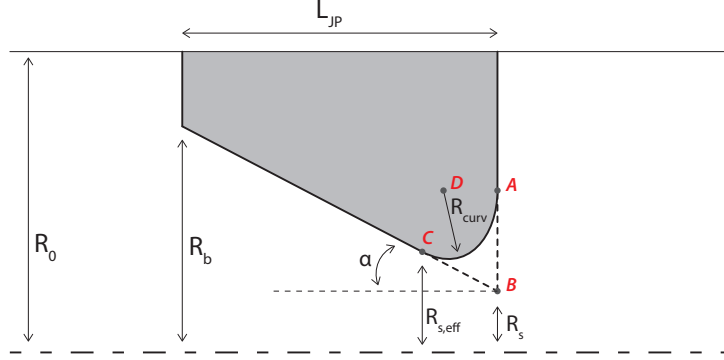


Figure 3.1: Jet pump with dimensions that fully define geometry [13].

$$A : \left[ 0; R_{curv} \frac{\sin \alpha + 1}{\cos \alpha} \right] \quad (3.3)$$

$$C : \left[ -R_{curv}(1 + \sin \alpha); R_{curv} \left( \frac{\sin \alpha + 1}{\cos \alpha} - \cos \alpha \right) \right] \quad (3.4)$$

$$D : \left[ -R_{curv}; R_{curv} \frac{\sin \alpha + 1}{\cos \alpha} \right] \quad (3.5)$$

Using the  $r$ -coordinate of point  $C$ , the effective small jet pump radius can be determined as follows:

$$R_{s,eff} = R_s + R_{curv} \left( \frac{\sin \alpha + 1}{\cos \alpha} - \cos \alpha \right) \quad (3.6)$$

This radius defines the highest velocity in the jet pump under the assumption of incompressible flow. In the case of a steady flow, the common way to calculate the pressure drop over the jet pump is by the formula shown in Equation (3.7) where  $K$  is a dimensionless minor loss coefficient,  $\rho$  is the density and  $u$  is the average flow velocity in the narrowest cross-section region.  $\Delta p_{observed}$  is the observed pressure drop over the change in cross-section while  $\Delta p_{ideal}$  is that same pressure drop but predicted from Bernoulli's principle [1].

$$\text{For steady flow:} \quad \Delta p_{minorloss} = \Delta p_{observed} - \Delta p_{ideal} = \frac{1}{2} K \rho u^2 \quad (3.7)$$

The minor loss coefficients,  $K$ , in Equation (3.7) are determined based on the cross-section transition, in this case the geometry of the jet pump. There is a minor loss coefficient defined for the sudden expansion in a tube as well as one for the sudden contraction of cross-sectional area. For the study of the jet pump, both openings, the big and the small cross-sectional area of the jet pump, require an expansion and a contraction minor loss coefficient. It is dependent on which way the flow is traveling whether an expansion or a contraction takes place, illustrated in Figure 3.2.

For the abrupt expansion certain assumptions need to be made to calculate the expansion minor loss coefficient. The velocity in the smaller pipe is assumed to be uniform over the cross-section,

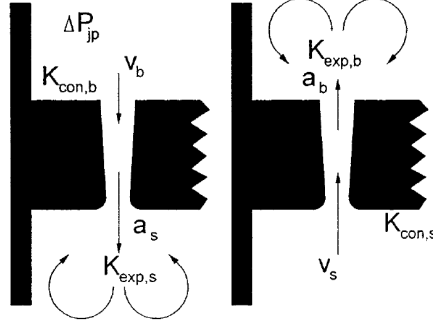


Figure 3.2: Schematic of the jet pump where both directions of flow are shown,  $v_b$  being the flow from big to the small opening and  $v_s$  the flow from the small to the big opening.  $a_s$  and  $a_b$  are the cross-sectional areas of the small and big openings respectively [18].

which only holds for high Reynolds numbers [4]. Variations in surface roughness of the pipe are neglected as the tangential force due to the boundary shear is not taken into account. At the transition cross-section the effect that the nonuniform velocity distribution has on the energy and momentum flux are not taken into consideration [5]. The values of  $\rho$  and the minor loss coefficients are independent of time [3]. With these assumptions the Borda-Carnot formula [1] can be used to calculate the expansion minor loss coefficients, shown in Equation (3.8).  $A_1$  is the cross-sectional area of the tube before the expansion and  $A_2$  is the area after the expansion as can be seen in the sketch in Figure 3.3. Based on the geometry of the jet pump, this results in the expansion coefficients shown in Equation (3.9), where  $A_{s,eff}$  is the cross-sectional area defined by the effective small radius;  $A_0$  is the cross-sectional area of the resonator tube; and  $A_b$  is the cross-sectional area of the big opening.

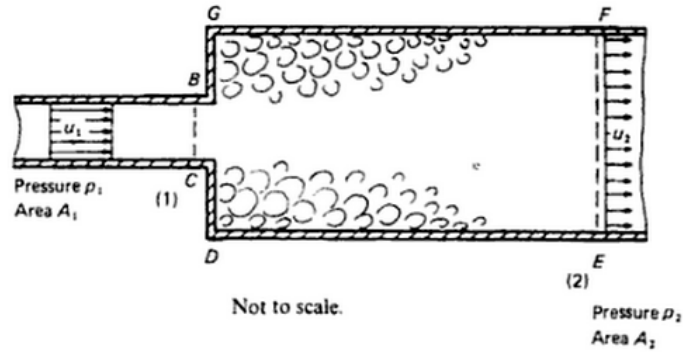


Figure 3.3: Sudden expansion in a pipe [4].

$$K_{exp} = \left(1 - \frac{A_1}{A_2}\right)^2 \quad (3.8)$$

$$K_{exp,s} = \left(1 - \frac{A_{s,eff}}{A_0}\right)^2 \quad \text{and} \quad K_{exp,b} = \left(1 - \frac{A_b}{A_0}\right)^2 \quad (3.9)$$

Although it seems likely that the values for the contraction coefficients are calculated in a similar manner because the geometry is simply the reverse of an expansion, this is not the case. As the flow is contracted into a smaller pipe the pressure varies at the junction in an unknown way and eddies are formed between the vena contracta which forms in the small pipe and the wall of the pipe [4], area  $A_c$  in Figure 3.4. This is where the energy is dissipated and this phenomena

is illustrated in Figure 3.4.

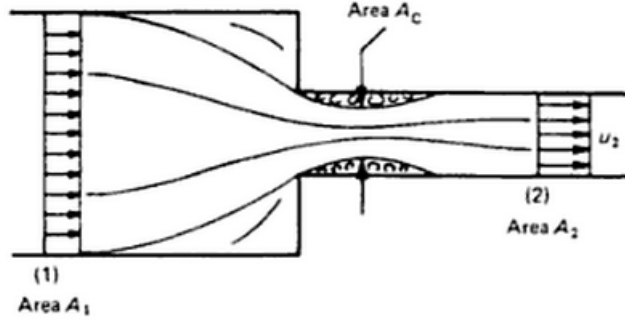


Figure 3.4: Sudden contraction in a pipe [4].

The curvature of the contraction determines the contraction coefficient and thus the values differ for the small and the big end, determined by their geometry. The big end is a sharp edge and thus the value of  $K_{con,b} \approx 0.5$  [18]. The coefficient  $K_{con,s}$  must be adjusted according to the radius of curvature, which is done by interpolating the data provided in the Handbook of Hydraulic Resistance [12]. The contraction coefficient is a value of 0.5 for sharp edges and will decrease as the edge becomes more rounded. When the radius of curvature ( $R_{curv}$ ) is such that  $\frac{R_{curv}}{2R_{s,eff}} \geq 0.15$  the value of  $K_{con,s}$  become approximately 0.04 [18].

The minor loss coefficients  $K_{con}$  and  $K_{exp}$  are defined for steady flow; however, they can be assumed to have the same values in oscillatory flow as they do in steady flow, based on the ‘‘Iguchi hypothesis’’ [1]. Iguchi and Ohmi [15] came to the conclusion that the results from their study of U-tube oscillations could be described by a quasi-steady approach. They were also able to show through extensive measurements that this quasi-steady approach is applicable in many situations involving high amplitude time-dependent flow [1]. Based on this assumption, and that the velocity in the jet pump is harmonic, Backhaus and Swift [18] derived a formula for the time-average pressure drop across a jet pump as found in Equation (3.10).

$$\Delta \bar{P}_{JP} = \frac{\rho_0 |U_1|_{JP}^2}{8A_s^2} \left( (K_{exp,s} - K_{con,s}) + \left( \frac{A_s}{A_b} \right)^2 (K_{con,b} - K_{exp,b}) \right) \quad (3.10)$$

This formula is used to determine the ideal geometry for the jet pump, as the effect of the various geometries on the time-averaged pressure drop over the jet pump is studied. The density and the speed of sound in the medium,  $\rho_0$  and  $c_0$  respectively, depend on the temperature in the set-up. These are determined by Equation (3.11) and (3.12), where  $\gamma = 1.4$  (specific heat ratio),  $R = 287.058$  J/kgK, and  $p_0 = 101325$  Pa (mean pressure).

$$c_0 = \sqrt{\gamma RT} \quad (3.11)$$

$$\rho_0 = \frac{p_0}{RT} \quad (3.12)$$

In the existing set-up the loudspeaker creates an acoustic wave. The voltage of the loudspeaker is related to the far field pressure, which is defined as the pressure amplitude where a plane wave is present. In this case this occurs in the resonator tube of the set-up. The pressure variation is equal to the amplitude of an oscillation. In a pure traveling wave, the far field velocity can be calculated directly from the far field pressure using:  $|u_1|_{FF} = \frac{|P_1|_{FF}}{(\rho_0 c_0)}$  and the volume flow rate is calculated using:  $|U_1|_{JP} = |u_1|_{FF} A_0$ . Given constant density, this volume flow rate is

a constant throughout the entire set-up as mass is conserved. Using the concept of constant volume flow rate, a ratio can be derived between the area of the small opening and the area of the tube of the set-up, see Equation 3.13 which only holds for a pure traveling wave. This relation is used to further derive the final Equation (3.16), which defines the small effective radius ( $R_{s,eff}$ ) of the jet pump that will be used further in the design of the jet pump.

$$\frac{|u_1|_{JP}}{|u_1|_{FF}} = \frac{A_0}{A_{s,eff}} \quad (3.13)$$

$$\frac{A_0}{A_{s,eff}} = \frac{R_0^2}{R_{s,eff}^2} \quad (3.14)$$

$$R_{s,eff} = \sqrt{\frac{R_0^2}{A_0/A_{s,eff}}} \quad (3.15)$$

$$R_{s,eff} = \sqrt{\frac{R_0^2}{\frac{|u_1|_{JP}}{|u_1|_{FF}}}}} \quad (3.16)$$

## 3.2 Restrictions on the design

In order to determine the design criteria of the jet pump, the existing set-up including the orifice, as described by Sam Lamboo [20], is used as a starting point. As the goal is to measure pressure drops over the jet pump as well as to clearly visualize the flow the most important criteria are the minimum value which can be obtained for the far field pressure and the maximum flow velocity through the jet pump. The far field pressure is restricted by the loudspeaker as it cannot go to very small pressure amplitudes and the pressure sensors signal-to-noise ratio gets too low at low pressure amplitudes. The maximum flow velocity is limited by the fact that it needs to be possible to take several photographs with the loudspeaker at approximately 100 Hz. If the flow velocity in the jet pump is too high it will be difficult to capture the flow with the camera at a shutter time of 1/1000 s and motion blur will result. To determine the specific restrictions on these two parameters a set of preliminary experiments are performed and can be found in Appendix 8.1. A summation of the most important restrictions that need to be taken into consideration when designing the jet pump are shown in Table 3.1.

Restriction	Reason
$\Delta P \gg 2.5$ Pa	accuracy of the manometer
$ P_1 _{FF} \gg 20$ Pa	volume of the loudspeaker
$ P_1 _{FF} < 3000$ Pa	range of the pressure sensor
$R_s < R_b < R_0$	principal of a jet pump
$R_0 = 30$ mm	existing geometry of the set-up
$L_{JP} < 180$ mm, $R_s \gg 1$ mm	scope of the 3D printer [11]
$max( u_1 _{JP}) = 1$ m/s	max velocity needed to make photographs at 20 Pa

Table 3.1: Restrictions and where they originate from

Based on the preliminary experiments the maximum for the velocity in the jet pump at a far field pressure of 20 Pa was chosen to be 1 m/s. The Honeywell pressure sensors which are installed at various positions in the set-up to measure the pressure amplitude cannot measure a pressure amplitude above the 3000 Pa. A minimum is set on the pressure amplitude which can

be read due to the analogue pressure gauge which has an accuracy of 2.5 Pa. The resonator tube is a set size which cannot be adjusted causing  $R_0$  to be set. A jet pump is designed according to the geometry presented in the previous section where the big radius of the jet pump is smaller than the radius of the resonator tube and the small radius of the jet pump is the smallest. The jet pump is to be 3D-printed and the company has certain criteria which the design must meet. The maximum bounding box which the printer can produce is 230x180x320 mm [11], restricting the length of the jet pump to 180 mm. As the product is also polished after production it is required that there is a minimum escape hole through which the powder can be removed from the product. This is a hole of 1 mm radius when there are two or more escape holes [11].

### 3.3 Jet pump design

The most important restrictions, the minimum far field pressure and the upper bound velocity in the jet pump, are used in order to determine an effective small radius that satisfy these. This can be done using Equation 3.16, giving an effective small radius of 6.7 mm.

For this effective small radius a corresponding big radius must be determined. This is done by calculating the time-averaged pressure drop versus the big radius for four different radii of curvature: 0.01 mm, 0.3 mm, 5 mm and 14 mm, see Figure 3.5. In this figure there are only three curves because the curve for the radius of curvature of 14 mm and that of 5 mm overlap, since the  $R_{curv}/D$  value which corresponds to these radii of curvature is larger than 0.15. All of the curves reach a maximum pressure drop and subsequently straighten out. This is due to the fact that as the big radius increases the ratio  $(A_s/A_b)^2$  becomes so small that the influence of the last term in Equation 3.10 is negligible. This maximum occurs once the big radius reaches a value of approximately 15 mm, then  $(A_s/A_b)^2 \approx 0.04$ , for all four curves. Realistically, the big radius cannot be 30 mm since this is the radius of the outer tube, thus a range of an appropriate big radius was chosen from 15 mm to 25 mm.

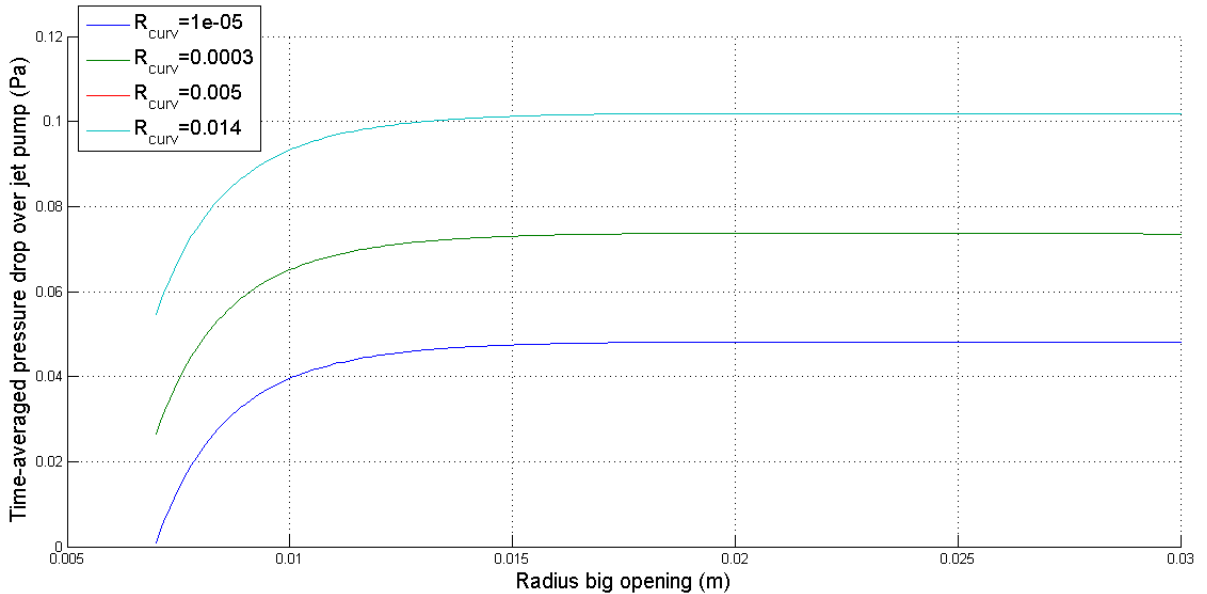


Figure 3.5: Time-averaged pressure drop against big radius for  $|P_I|_{FF} = 20Pa$ .

The next important geometrical attribute to consider is the radius of curvature. In order to determine the influence of the radius of curvature on the pressure drop, a value for the big radius is chosen and the effect of varying the radius of curvature is considered. From Equation (3.6)

it is noted that the radius of curvature only influences  $K_{exp,s}$  and  $K_{con,s}$ . The value of  $K_{con,s}$  decreases with increasing radius of curvature but once a value of  $R_{curv}/D$  greater than 0.15 is reached  $K_{con,s}$  will remain 0.04. Correspondingly, the pressure drop has reached a maximum at this value, which occurs at a radius of curvature of approximately 2 mm. Any value larger than this will result in the same maximum pressure drop, thus a radius of curvature of 5 mm is chosen for convenience in material choice. The ideal big radius can be chosen by considering the length of the jet pump and the design restrictions.

For the length of the jet pump the restriction due to manufacturing is 180 mm, however, ideally the jet pump is chosen as short as possible in order to minimize the costs but yet long enough to have a small taper angle. The bigger the taper angle the more chance that the experimental results will not match the analytical model as predictions of the flow cannot be made as easily. The length of the jet pump can be calculated using Equation (3.17), where the small radius  $R_s$  is defined as in Equation (3.18).

$$L_{JP} = \frac{R_b - R_s}{\tan(\alpha)} \quad (3.17)$$

$$R_s = R_{s,eff} - R_{curv} \left( \frac{\sin\alpha + 1}{\cos\alpha} - \cos\alpha \right) \quad (3.18)$$

The angle that is chosen to calculate the length is  $\alpha = 7$  deg which is chosen based on the experimental results of Petculescu [1]. An appropriate big radius is 15 mm as it is the minimum value which results in a significant pressure drop as seen in Figure 3.5 and when filled into Equation (3.17) it results in a realistic length of 70.76 mm.

Ideally, a significant pressure drop can be measured (greater than 2.5 Pa) over the jet pump with a velocity in the jet pump that ranges around the 1 m/s. This represents the desired window in which the pressure drop can be measured and photographs can be taken of the flow. The final jet pump geometry is seen in (3.19) which theoretically results in a pressure drop shown in Figure 3.6. The range of far field pressures which will be needed is from 20 to 200 Pa which corresponds to a far field velocity of 0.0484 m/s to 0.484 m/s.

$$\begin{aligned} R_{s,eff} &= 7 \text{ mm} \\ R_s &= 6.3 \text{ mm} \\ R_{curv} &= 5 \text{ mm} \\ R_b &= 15 \text{ mm} \\ L_{JP} &= 70.76 \text{ mm} \\ \alpha &= 7 \text{ deg} \\ |P_I|_{FF} &= 20 \text{ to } 200 \text{ Pa} \\ |u_I|_{FF} &= 0.0484 \text{ to } 0.4838 \text{ m/s} \end{aligned} \quad (3.19)$$

A sensitivity study is performed in order to determine the influence of temperature on the mean pressure drop. The temperature in the set-up varies as the loudspeaker heats up, giving an average error of 2.35% with a temperature fluctuation of 5°C.

### 3.4 Simulation of flow field

In order to get insight into whether or not there will be visible differences in flow patterns at the various velocities it is of interest to create a computational fluid dynamics model of the set-up. Especially for the flow visualization it is interesting to study the vortices and jetting which form due to the jet pump. Using COMSOL Multiphysics v4.4 the behaviour of the jet pump

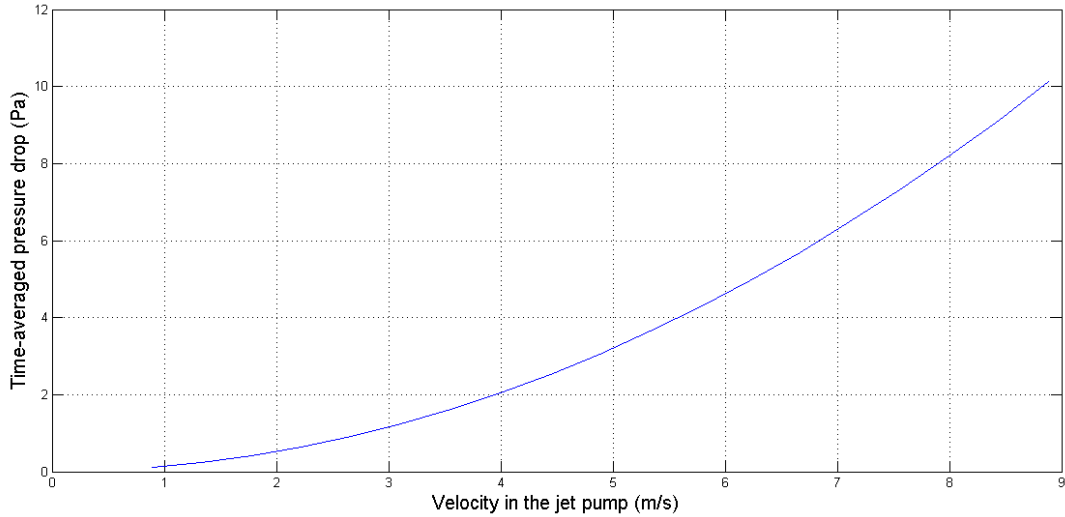


Figure 3.6: Analytical model of the time-averaged pressure drop against velocity in the jet pump.

is simulated using the geometry and the conditions defined above, see the set of parameters in 3.19. The flow is specified as an incompressible, isothermal oscillating flow and the end of the set-up is simulated as being completely open. The simulation is performed for sixteen different far field velocities ranging between 0.05 and 1.5 m/s. All further references to COMSOL simulations refer to results obtained by Joris Oosterhuis, where details on the specifications of the simulations are described by Oosterhuis [13].

Figure 3.7 shows the flow vorticity at a far field velocity of 0.05 m/s and Figure 3.8 shows the flow vorticity at 1.5 m/s. These are the maximum and minimum velocities which were simulated and the differences in flow patterns are very clear. At a low velocity no vortices are formed while at the higher velocities counterclockwise turning (red) as well as clockwise turning (blue) vortices are present. The scale on the right hand side also shows that the vorticity is 20 times stronger at high velocities. The four plots show the flow field at four different phases, clearly illustrating the movement of the vortices from left to right in Figure 3.8. When comparing all the simulation results for a range of velocities it becomes clear that the vortices start to form at a far field velocity of around 0.2 m/s and increase in vorticity as the far field velocity is increased. It is predicted that this is what will occur in the experiments.

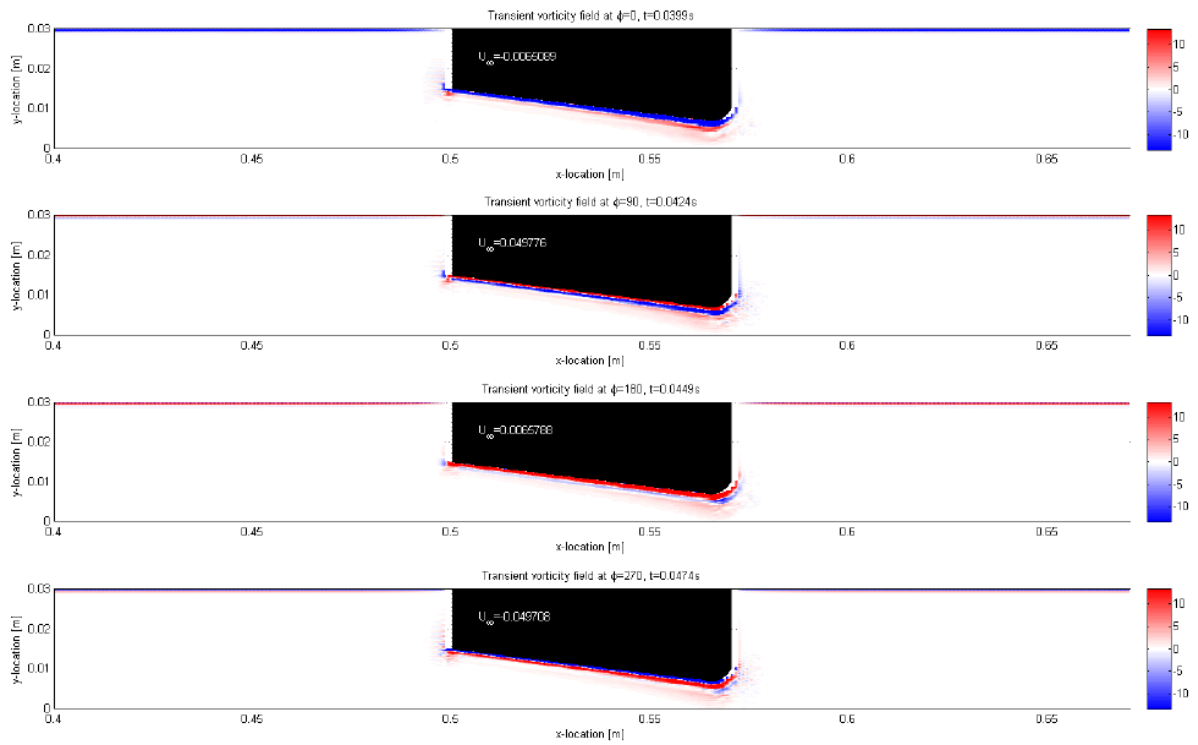


Figure 3.7: Transient vorticity field for four different phases at a far field velocity of 0.05 m/s.

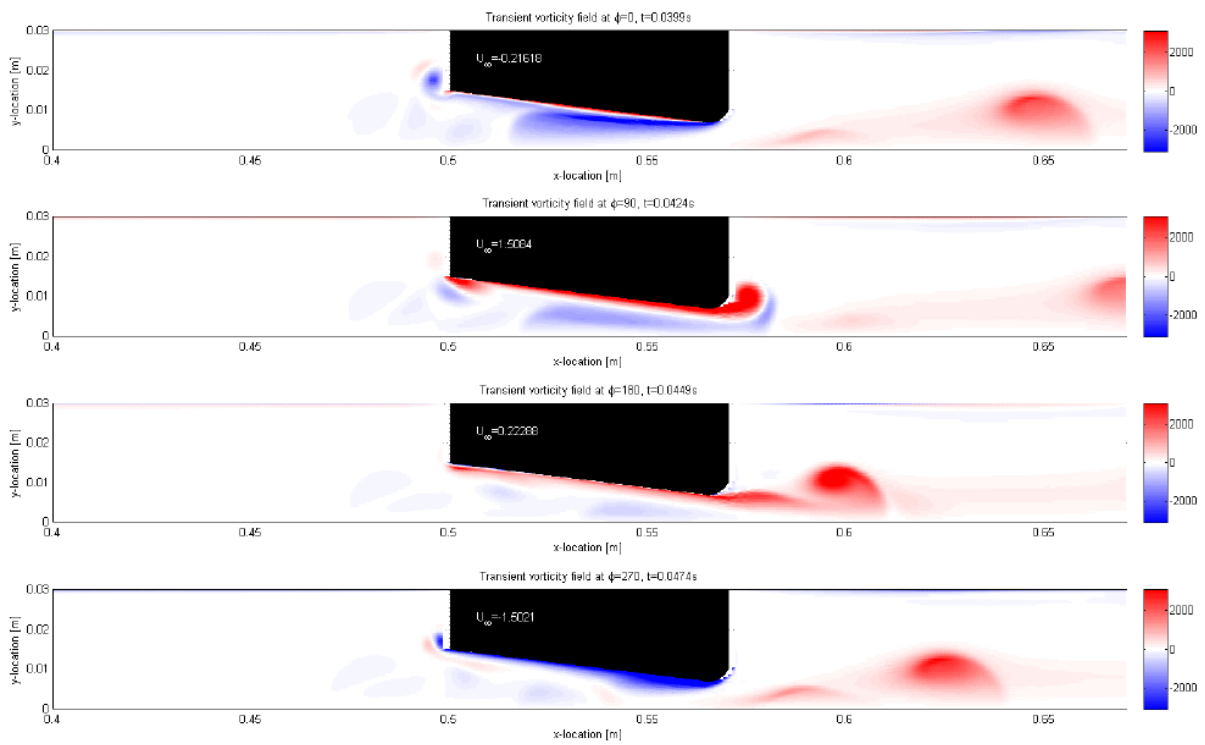


Figure 3.8: Transient vorticity field for four different phases at a far field velocity of 1.5 m/s.

## 4 Experimental set-up

### 4.1 Existing set-up

The experimental set-up that is used throughout this experiment was constructed in the Thermal Engineering research group at the University of Twente. For completeness an overview of the set-up is provided in addition to a more detailed description provided by Paul Aben [16]. A model of the set-up is shown in Figure 4.1. The main elements of the construction are a loudspeaker, a cone and a resonator part. The resonator tubes are separate aluminium cylindrical tubes which can be connected together, allowing for the addition of other sections and alterations in length. In this case a section is added that contains the jet pump while for other research a parallel-plate temperature stack is inserted for temperature and pressure experiments. The right end of the resonator tube is connected to a cone and a loudspeaker with a closed back. The loudspeaker creates an acoustic wave which is amplified by the large transition in diameter from the cone to the resonator. The left hand side can be altered to provide different reflection coefficients by leaving it open (reflection coefficient of  $-1$ ), closing it off (reflection coefficient of  $+1$ ), or attaching a resonator termination which is designed with a reflection coefficient of  $0.04$  at  $113$  Hz. When the resonator termination is attached an almost perfectly traveling wave is present in the set-up while otherwise a standing wave is formed due to the reflections.

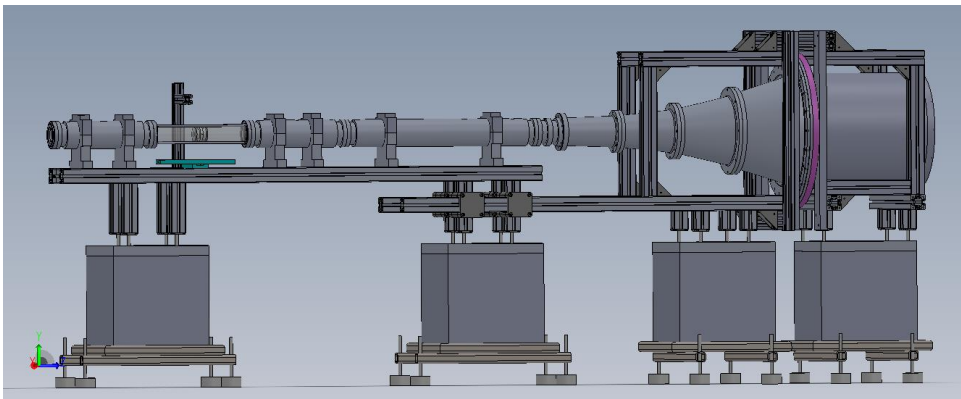


Figure 4.1: Model of the existing set-up including jet pump section.

The jet pump is inserted into a  $480$  mm long acrylic glass (PMMA) tube with an inner diameter of  $60$  mm and a supporting structure is fitted around it so that it is compatible with the existing resonator tubes. The supporting structure consists of two flanges and four aluminum bars of  $380$  mm. In order for the flow to be easily visualized the tube is made from a transparent material: PMMA. PMMA is a good material to work with as it is also cheaper and less fragile than glass. Figure 4.2 shows a model of the jet pump test section.

In order to perform the flow visualization experiments and pressure measurements several components are added to the set-up as previously described. These include the camera, the smoke generator, the laser, the pressure sensors and the differential pressure gauge.

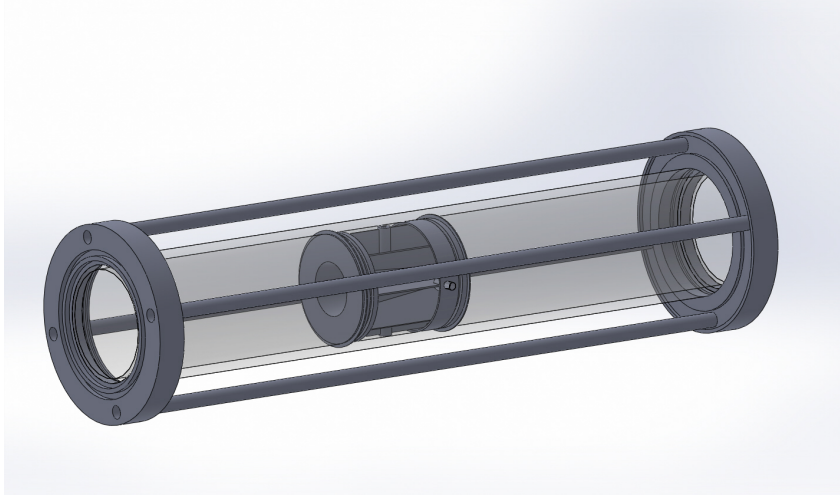


Figure 4.2: Jet pump test section.

#### 4.1.1 Camera

A Nikon D5200 camera with a Nikkor 40mm Micro lens is used for the photographs during flow visualization. The lens is capable of taking photographs up to a 1:1 scale. The three settings which are essential for controlling the exposure of the photographs are the shutter time, the aperture and the ISO rating. The Nikon D5200 is able to take photographs with a shutter time of up to 1/4000 second. A high shutter time means that several photographs can be taken per period of the oscillating flow, however, a lot of light is required. This needs to be balanced out by the aperture which ranges from  $f/2.8$  to  $f/22$  for the Nikkor lens and the ISO rating which ranges from ISO 100 to ISO 25,600 for the Nikon camera.

#### 4.1.2 Laser

The laser that is used in the experimental set-up is a line laser. A line laser is a point laser which in combination with optics creates a line instead of a point. Between the diode which emits the laser beam and the line which is created a thin light sheet is formed that illuminates a 2D plane. The laser sheet will thus create a cross-sectional view of the flow making it a convenient method to visualize vortices [7]. The laser which is incorporated in the set-up is a 5mW, 635nm Laserlyte Flex continuous dot laser with interchangeable lenses. A single lens is used which projects a line at a 90 degree fan angle [20].

#### 4.1.3 Smoke generator

In previous experiments four different smoke generators had been considered and evaluated based on the experimental needs [20]. The best option turned out to be using a model train smoke generator which was inspired by the use of model train oil for the smoke-wire technique [9]. A model train smoke generator, shown in Figure 4.3, produces smoke by heating lamp oil with a heating element as an electrical current is passed through. A fan sucks air from the atmosphere to direct the smoke out of two exhausts located at the top of the smoke generator. One of the exhausts is closed off so as to direct all the smoke out of the other exhaust via a plastic tube into the jet pump. The 12V smoke generator measures 55x40x55 mm and runs on lamp oil to produce a denser smoke than model train oil. The main advantages of the model train smoke generator over other options are: small amounts of smoke are produced, the generator itself is small and easily fits in the set-up, the smoke can be inserted directly into the desired region, smoke generation is continuous, the smoke is white and well visible, and does not condensate rapidly or leave behind undesired particles [20].

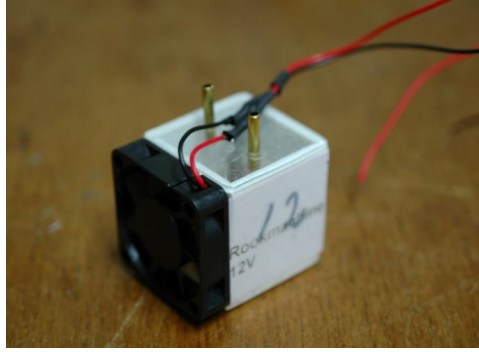


Figure 4.3: Model train smoke generator [20].

#### 4.1.4 Pressure sensors and pressure gauge

In order to perform pressure measurements in the set-up two different techniques are used so that the results can be compared: digital pressure sensors and an analogue differential pressure gauge. Both of these methods can be used to measure a mean pressure at a specific position in the set-up as well as a pressure difference between two points.

The pressure sensors which are used are Honeywell piezoresistive pressure sensors and are mounted in the set-up using a custom designed 3D printed mount, seen in Figure 4.4. The mounts are made such that the bottom surface matches the curvature of the tube and can be mounted flush with the inside wall of the set-up. There are several points in the set-up at which these sensors can be attached. A capillary of 2 mm diameter samples the pressure and the sensor membrane itself is placed approximately 17mm inside the sensor housing. The back pressure port of the sensor is exposed to the ambient pressure. The data collected by the pressure sensors is relayed to the computer in the form of the pressure amplitude per sensor as well as the mean pressure per sensor.

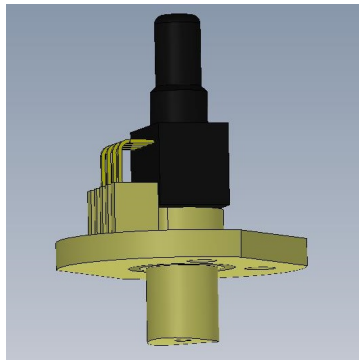


Figure 4.4: Honeywell pressure sensors with mount.

Three Dwyer Magnehelic Differential Pressure Gauges are also mounted to the set-up each with a different scale: 0 to 0.25 inch WC; 0 to 1 inch WC; 1 to 10 inch WC. The units on the differential pressure gauges are in inch water column where one inch water column is equal to 248.84 pascals. Since these gauges are not as compact as the pressure sensors they cannot be mounted in the set-up and instead are connected via a flexible hose, as seen in Figure 4.5. The benefit of these pressure gauges is that they can measure a pressure drop between two points without being effected by oscillations in the flow as their response time is typically larger than a wave period [2]. Throughout this paper the differential pressure gauges are also referred to as manometers.

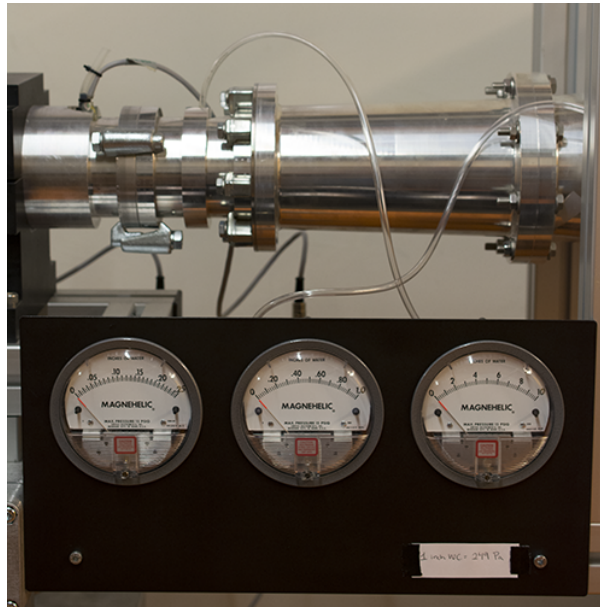


Figure 4.5: Differential pressure gauge mounted to set-up.

## 4.2 Pressure measurements

The main goal of this assignment is to perform pressure measurements with the jet pump and to visualize the flow through the jet pump. The pressure measurements are performed using two different methods of measuring: the differential pressure gauge and the digital pressure sensors as described in Section 4.1. Both devices can be installed in the set-up at seven different points in order to measure the pressure at various positions in the flow. In section 4.2.1 the results of a range of pressure measurements using these two different techniques are presented and discussed. These tests are performed to determine whether there are significant differences in the values returned and whether the installation of the differential pressure gauge affects the flow in the set-up. It was also observed during previous experiments that there is a mean pressure build up in the set-up [8]. In section 4.2.2 this is investigated as well as the effect of installing a needle valve in order to remove this mean pressure build up.

### 4.2.1 Comparison of sensors and differential pressure gauge

Prior to carrying out the pressure measurements of the time-averaged pressure drop over the jet pump, it is necessary to evaluate the consistency and conformity of the Honeywell piezoresistive pressure sensors and the Dwyer Magnehelic Differential Pressure Gauges. The termination of the resonator tube, the presence of the jet pump section and the position of the manometer and pressure sensors are investigated.

Measurements of the mean pressure differences over an empty tube using two different terminations are made to see whether the manometer and the pressure sensors display similar trends and conformity. A pressure sweep is done from 0 to approximately 150 Pa as well as from 150 to 0 Pa, in order to see if the trends are really dependent on the pressure amplitude, for the set-up with a closed end and with the resonator termination. Figure 4.6 illustrates the results of this pressure sweep as measured by the manometer and the sensors, where the manometer resolution is 0.625 Pa. For clarity it was chosen to only display the mean pressure difference

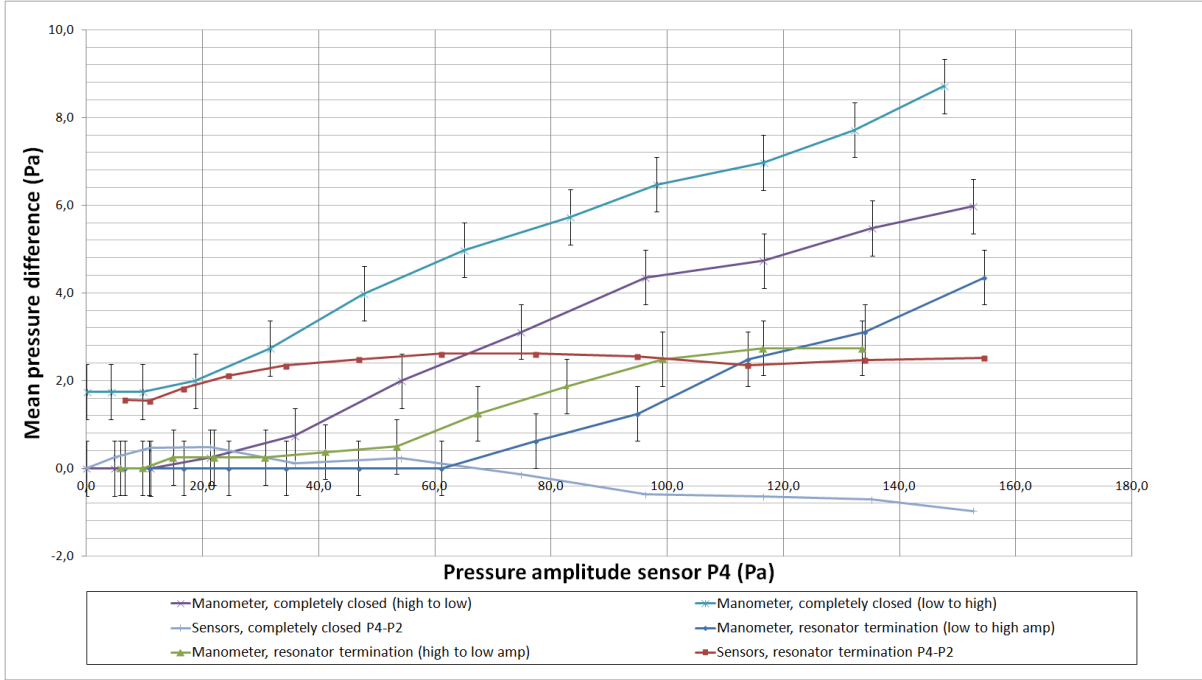


Figure 4.6: Mean pressure difference over an empty resonator tube with and without a manometer attached.

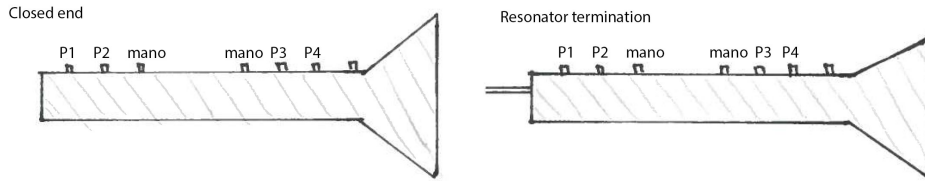


Figure 4.7: Sketch of the position of the pressure sensors and manometer.

between sensor P3 and P4, see Figure 4.7.

Since there is no jet pump inserted, the mean pressure difference between two sensors in the empty tube is expected to be zero. The pressure sensors in the case of the closed end fluctuate by approximately 1 Pa around a value of 0 Pa. For the resonator termination the sensors measure a mean pressure difference that fluctuates around 2 Pa also with a maximum of 1 Pa deviation. The resonator termination does have an affect on the pressure difference, however, this effect is minimal. The difference in trend between the manometer measurements and the pressure sensors is clear in both cases: the pressure sensors remain almost constant while the manometer measures an increasing mean pressure difference. This difference could be a result of the fact that the acoustic impedance of the tap (the connection between manometer and set-up) is not large enough. Hence, the pressure oscillations produced by the loudspeaker can lead to a oscillatory flow velocity through the tap, which influences the mean pressure reading. Streaming and jets also form at such a tap, which leads to a mean pressure difference which is nonzero [2]. Based on the tests done by Smith [2], this jetting effect at the tap is expected to be the strongest in regions of high pressure amplitude. These pressure nodes are investigated further.

Using the acoustic model [8] the pressure amplitude is calculated against the position in the set up and plotted in Figure 4.8. The calculations are performed for a set-up with a closed end

running at 100 Hz with a 10 V input voltage. In Figure 4.8 the pressure antinode at  $x = 1.819\text{m}$  and pressure node at  $x = 2.683\text{m}$  are marked, where  $x = 0\text{m}$  refers to the back volume and  $x = 2.683\text{m}$  is the end of the set-up. The maximum pressure amplitude (antinode) is thus measured at the end of the set-up while the minimum pressure amplitude (node) is measured at 86.4 cm from the end of the tube.

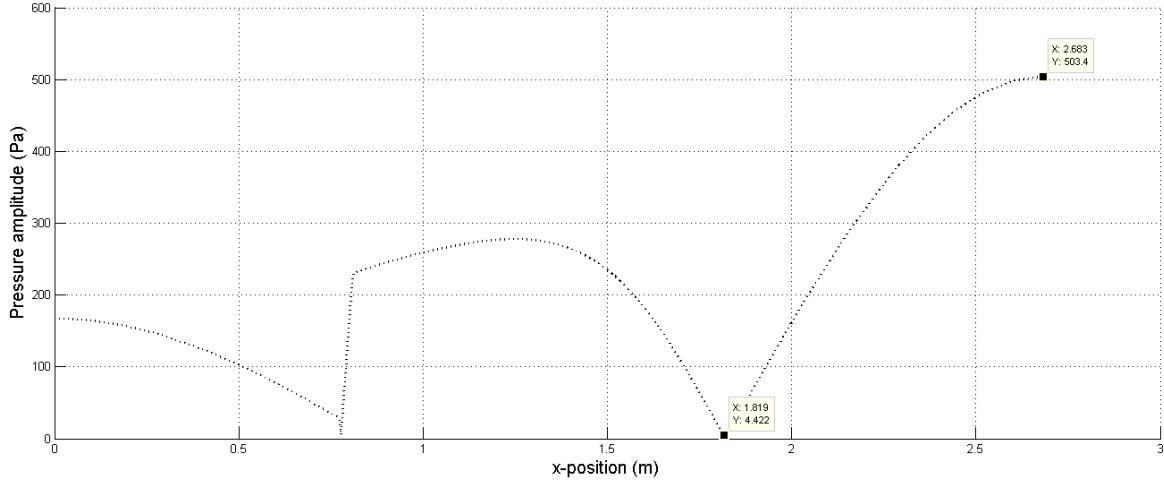


Figure 4.8: Model of the pressure amplitude over the position in the set-up.

The mean pressure is measured at the antinode as well as the node, with the end of the set-up closed, by both the pressure sensors and the manometer positioned as shown in Figure 4.9. One end of the manometer is attached to the set-up while the other is open to the environment. A pressure sweep from 0 to approximately 1900 Pa is performed at a frequency of 100 Hz. The mean pressure at sensor P1 is plotted for the antinode and that of P4 for the node, against the reference pressure amplitude at sensor P2, see Figure 4.10.

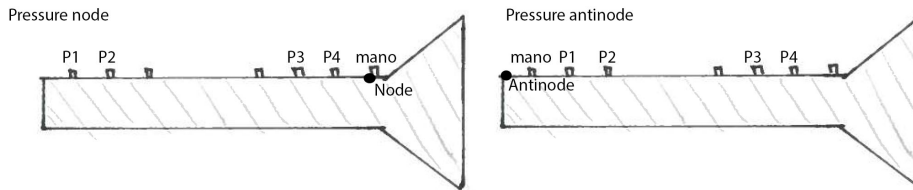


Figure 4.9: Sketch of the position of the pressure sensors and manometer, with the node and antinode marked by a black dot.

The four curves display similar trends, as they all start off constant between 0 and 10 Pa and then display a seemingly quadratic increase. As is expected according to Smith [2], at the pressure node the manometer results are in good agreement with the pressure sensor results with a maximum deviation between the two of around 10.7% and an average deviation of 8%. At the pressure antinode where the pressure amplitude is maximum the manometer results differ more from the pressure sensor results with a maximum deviation of around 20% and an average deviation of 11%. These results are only for a maximum pressure amplitude of approximately 2000 Pa. Smith observed a higher deviation, however, his measurements were performed up to 8000 Pa and only started displaying a significant difference after 2000 Pa. It is predicted that at higher pressure amplitudes the values at the antinode will differ more for the manometer and the pressure sensors as is. For further pressure measurements the manometer and the pressure

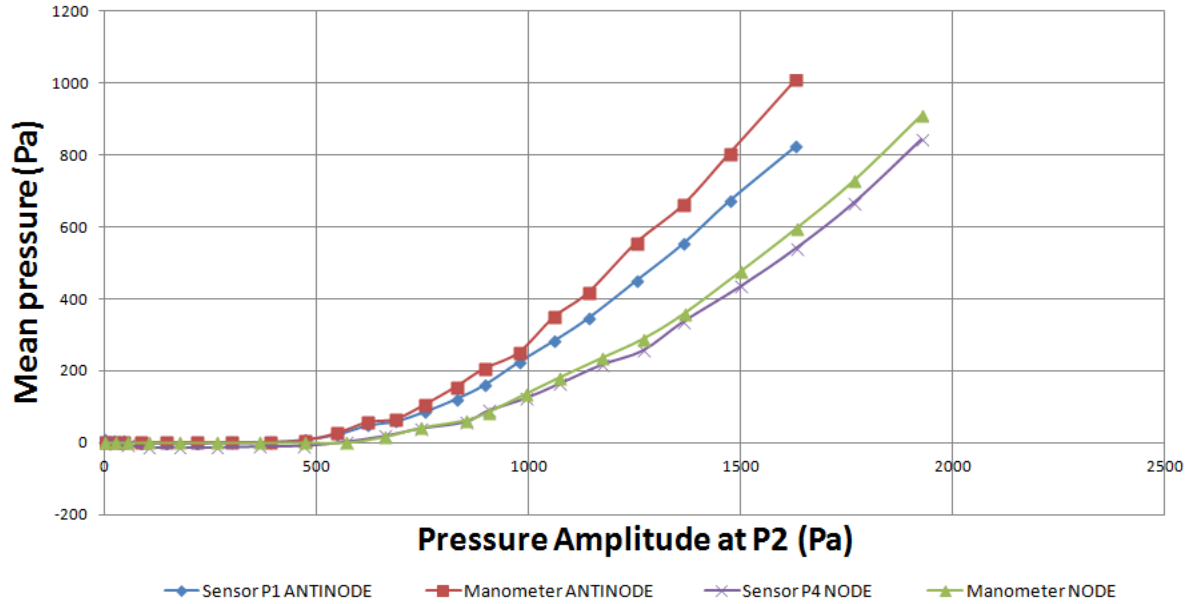


Figure 4.10: Mean pressure drop at the pressure node and antinode in an empty tube.

sensors are both used to measure the time-averaged pressure drops to compare the results.

#### 4.2.2 Regulation of mean pressure

During previous experiments [8] it was observed that there is a mean pressure build up in the set-up due to the increase in temperature of the loudspeaker. The mean pressure in a closed set-up without the resonator termination attached is measured over time, at a pressure amplitude of 260 Pa running at 113 Hz, to observe this trend. The plot in Figure 4.11 shows the mean pressure measured over time by the four different pressure sensors and the manometer positioned as is shown in the sketch in Figure 4.12. The pressure amplitude is measured at five different positions in order to determine whether the mean pressure increase is position dependent or not.

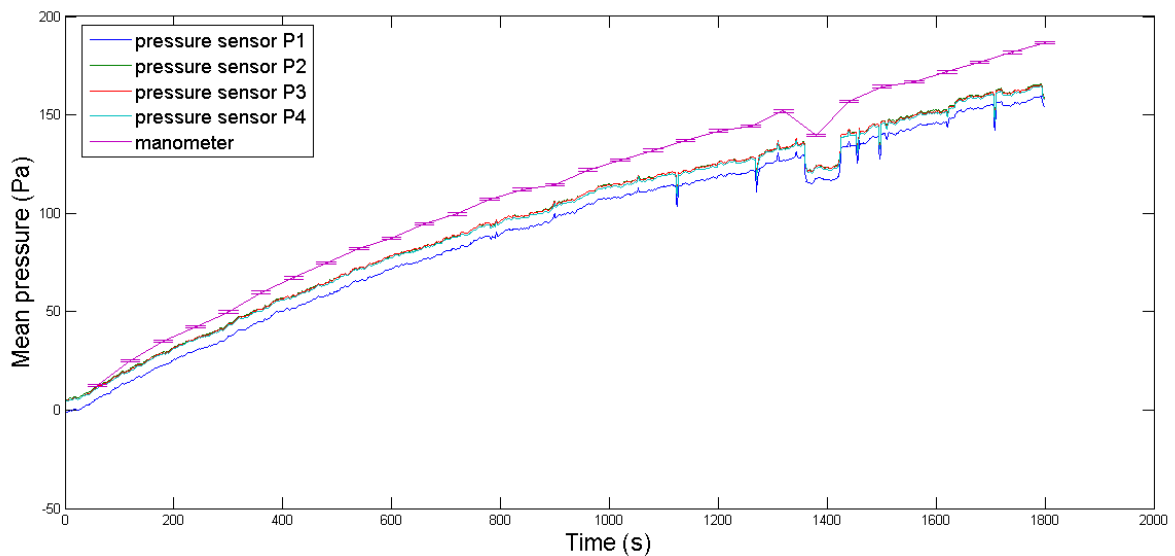


Figure 4.11: Mean pressure in the empty resonator as a function of time.

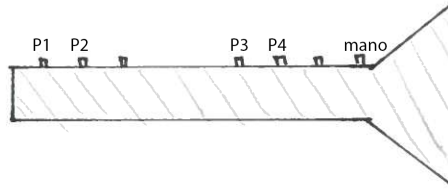


Figure 4.12: Sketch of the position of the pressure sensors and manometer.

Figure 4.11 indicates that the mean pressure at all four positions increases with time. The mean pressure measured by pressure sensor P4 differs significantly with the other three pressure sensors. Since the other three sensors do not start at zero at time  $t = 0$ , it is most likely a calibration error as the trend of all four curves are identical. The mean pressure measured by the manometer lies significantly higher than those measured by the four pressure sensors. The dip which is viewed in all the curves is probably a result of an atmospheric change such as someone closing or opening the door of the laboratory. When the loudspeaker was turned off and the resonator was opened a sound of abruptly flowing air was heard at the opening. This reinforces the initial suggestion that there is a mean pressure build up in the set-up due to the loudspeaker which is producing acoustic waves.

This mean pressure build up will influence the results of the pressure measurements and makes it more difficult to get smoke inside of the set-up during flow visualization tests. A way to regulate the mean pressure in the set-up is by using a pressure valve to continuously release some air. To investigate the effect of a pressure valve on the mean pressure various tests with a range of terminations of the resonator are performed. For all the following tests the positioning of the sensors is as in the sketch in Figure 4.13 where the last port on the left hand side is varied from closed, open and with a needle valve attached.

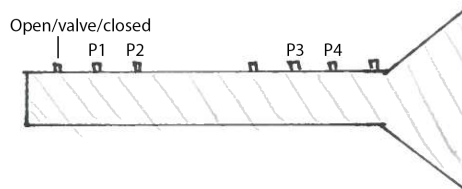


Figure 4.13: Sketch of the positioning of the pressure sensors, where the last port is varied between closed, open and with a needle valve attached.

The type of pressure valve used for this experiment is a needle valve as it allows for precise regulation of flow and is usually used for low flow rates. The purpose of the needle valve is to keep the mean pressure at zero. At a pressure amplitude of 200 Pa with the set-up running at 100 Hz the mean pressure build up is studied for three cases: closed end with needle valve completely open, closed end with last hole completely open, and a completely closed end. The plots of these three situations are overlaid for easy comparison of scale and noise level in Figure 4.14.

In both the set-up with the hole open and the needle valve open the mean pressure is constant over time compared to the case with the end completely closed, as seen in Figure 4.14. In the set-up with the hole open the mean pressure measured at sensor P1 fluctuates while the other three sensors are constant. This sensor is located closest to the opening and thus the mean pressure fluctuations could be caused by streaming effects through the opening. The mean pressure

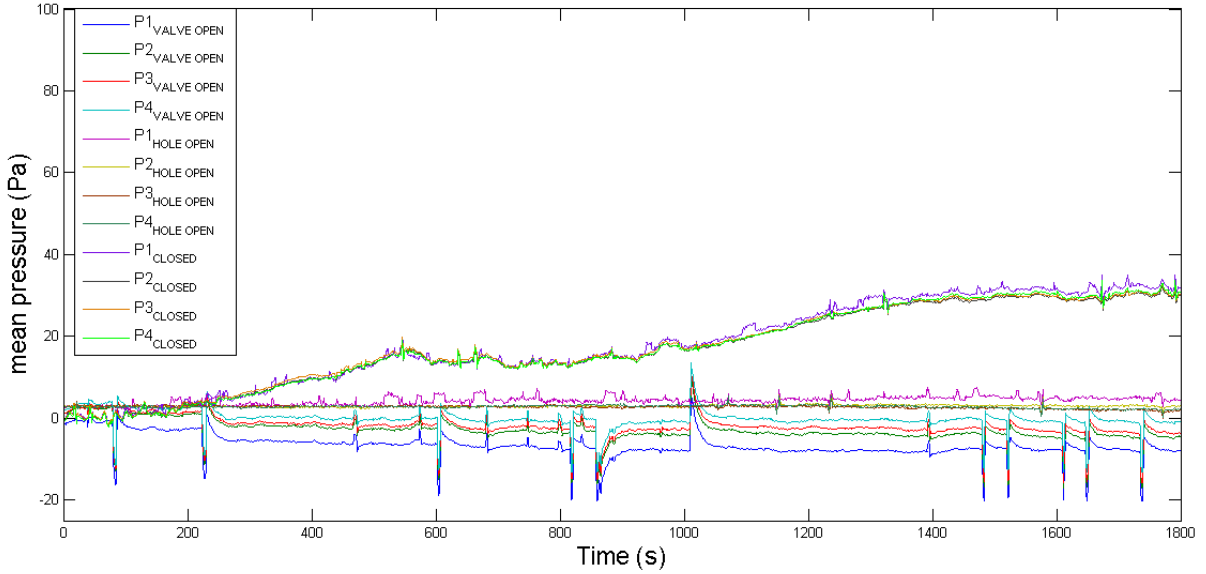


Figure 4.14: Mean pressure over time for: closed end with needle valve completely open, closed end with last hole completely open, and a completely closed end.

measured in the set-up with the needle valve open displays four identical mean pressure curves only starting at a different value at  $t = 0$ . There is a significant amount of noise in these results and the peaks which occur are large compared to those in the other two curves. The same trend as the plot in Figure 4.11 is identified in the curve of the closed end as it is the same test only performed at a pressure amplitude of 200 Pa for comparison. From these three tests it can be concluded that both the needle valve and the open hole result in a zero mean pressure, however, the needle valve seems to be affected more by streaming effects through the opening.

With the use of a spindle the flow that passes through the needle valve can be regulated. This works by turning the screw, which retracts the plunger and thus allows flow to pass between the plunger and the seat. The sensitivity of this instrument is not known and in order to observe how much influence the opening of the valve has, a test is performed. The set-up is run at 100 Hz at a pressure amplitude of 200 Pa and every two minutes the needle valve is opened by one cycle on the spindle. Figure 4.15 shows the mean pressure measured with the needle valve regulated over time where the valve is closed at  $t = 0$ s, completely open at time  $t = 1320$ s, and fully closed again at  $t = 2760$ s. The plot of the mean pressure build up in the closed set-up at 200 Pa is overlaid in order to compare the slopes of the two curves.

As expected the mean pressure in the set-up increases when the needle valve is closed at  $t = 0$ s up until when it is open completely  $t = 1320$ s. The slope of the closed set-up (approximately 0.038 Pa) is very close to the slope when the needle valve is being opened in the first 1,320 seconds (approximately 0.030 Pa). This suggests that the opening of the needle valve has little effect on the flow until the needle valve is completely opened, which occurs at  $t = 1320$ s. At this instant in time the mean pressure drops almost immediately to zero and remains almost constant until the valve is closed again at  $t = 2760$ s. At this point pressure sensor P1 continues to follow the same trend, with an increasing slope, while the other three sensors suddenly drop to a negative mean pressure and then display the same increasing trend. This could be due to streaming effects near the exit of the valve but this was not observed with the valve completely open and the setup completely open, so the reason remains unknown. All four sensors do indicate, however, that the mean pressure builds up in the set-up once the valve is closed only slightly, reinforcing the suggestion that the needle valve only has an influence when it is

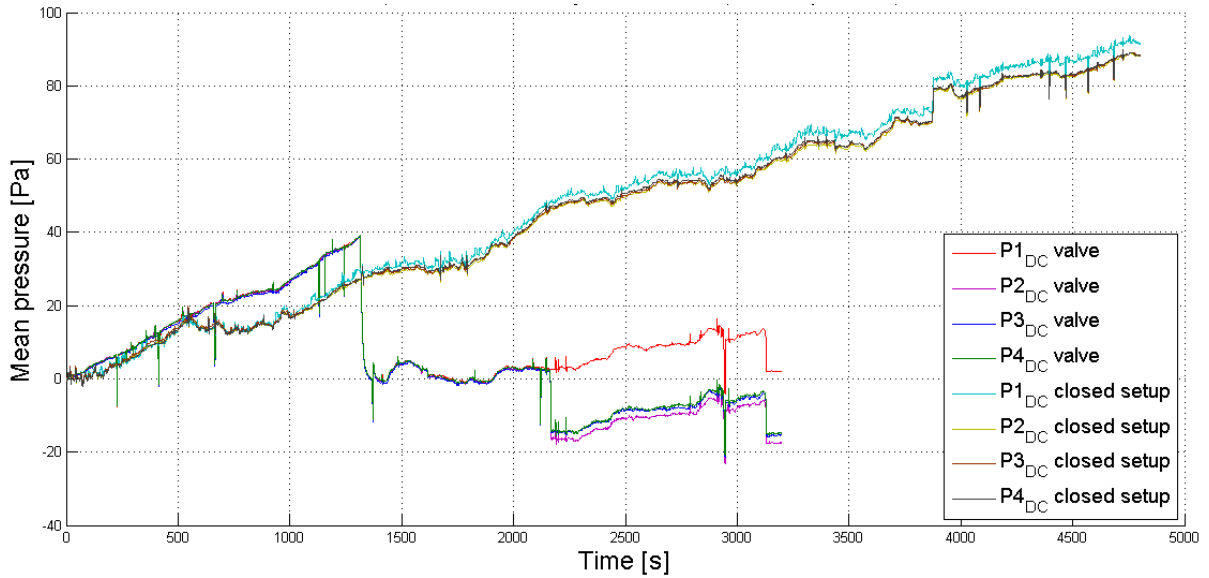


Figure 4.15: Mean pressure measurement with regulated needle valve over time and mean pressure build up in closed set-up, both at 200 Pa.

completely open or completely closed.

A final test is performed to confirm this suggestion with the set-up completely closed and the needle valve attached to the end. The mean pressure is built up to 1000 Pa with a starting pressure amplitude of 1000 Pa with the set-up running at 100 Hz. Once this mean pressure has been reached in the set-up, the loudspeaker is turned off and every two minutes the pressure valve is opened by one cycle.

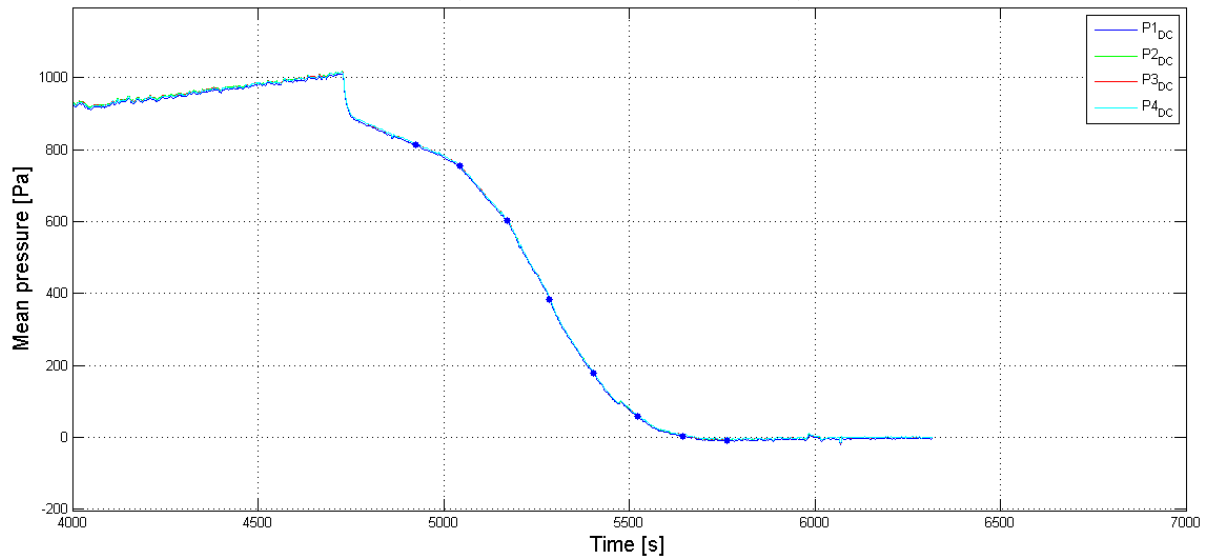


Figure 4.16: Mean pressure measurement with regulated needle valve over time starting at a mean pressure of 1000 Pa.

In Figure 4.16 the mean pressure is plotted against time with the points at which the pressure valve was opened by one cycle marked on the curve. The mean pressure with the valve closed is allowed to build up to 1000 Pa and at  $t = 4800$  sec the set-up is turned off. The mean pressure

in the set-up immediately drops and then the slope starts to level out until the needle valve is opened for the first time after two minutes at  $t = 4920$  sec. It is observed that the slope changes only slightly after each opening of the needle valve, however, in order to determine the influence of this opening it should be overlaid with a test under the same conditions but then without the needle valve.

From all the tests performed in can be concluded that the sensitivity of the needle valve is not enough to regulate the flow other than by opening the valve completely or closing it completely. The pressure measurements which were done do not lead to conclusive evidence as to whether the needle valve has less influence on the flow than opening the hole at the end of the set up. It is necessary to compare the acoustic field before being able to conclude anything about the needle valve. The exact influence on the flow is something which can also be observed using flow visualization techniques in order to see whether or not there are streaming effects around the valve opening. However, it can be concluded that both the needle valve and the open hole keep the mean pressure build up to a minimum.

### 4.3 Flow visualization

Using computational fluid dynamic models produced in COMSOL it is possible to predict certain flow patterns caused by the jet pump as was presented in section 3.4. These simulations provide predictions of the strength of the vortices which will form over time at specific flow rates. It is desirable to determine experimentally whether or not these predictions are correct and to be able to capture this visually. To perform this flow visualization the smoke generator, the 5mW laser, and the Nikon D5200 camera as described in section 4.1 are used. The exact positioning and the working of these three elements is described in the following section following an explanation of the method of smoke injection into the set-up. Although a Nikon D5200 camera is used for the final flow visualization experiments, a number of tests are also presented which are done with a Phantom v7.3 high speed camera.

#### 4.3.1 Smoke injection

The jet pump geometry was determined based on a literature study and the analytical model as described in section 3.3. The next important step in the design of the jet pump is the smoke injection. Due to ease in manufacturing and accuracy of production it was chosen to 3D-print the jet pump, with the material PA2200, a strong and flexible plastic [11].

From previous research it was concluded that the position of the smoke inlet has a significant influence on the symmetry of the smoke flow which is entering the set-up. Therefore, it was recommended to design a smoke inlet which is more symmetrical [20]. Other aspects that need to be considered when designing the smoke inlet is that the smoke has the least influence on the flow if it is inserted where the flow velocity is a maximum. In addition it is favorable that the inner surface of the jet pump is not altered by introducing large holes so the flow is not disturbed while passing through the jet pump. These three observations led to the idea of the smoke being inserted at an angle to the flow instead of perpendicular as was done previously. By creating the hole where the smoke is inserted on the face of the jet pump instead of inside the jet pump it is assumed to have less effect on the flow and the inside of the jet pump is not altered. This concept can be tested by doing a preliminary experiment using the existing set-up with the orifice instead of the jet pump. A hole was created on the face of the orifice as seen in the sketch in Figure 4.17 and the existing hole was closed off so that no smoke could exit. Subsequently tests were performed using this new orifice at a frequency of 100 Hz and with the

loudspeaker at a voltage of 0.44 V. An image taken with a shutter speed of 1/1000 seconds, an aperture of F/3.2 and an ISO rating of 25,600 is shown in Figure 4.18 compared to an image of smoke flow in the existing set-up at the same settings. The orifice opening is seen on the left hand side of both photographs while the smoke is inserted as shown in Figure 4.17.

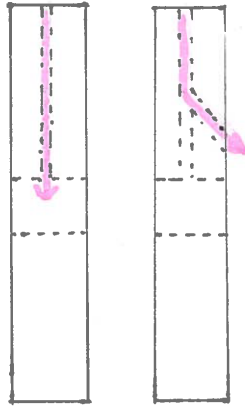


Figure 4.17: left: existing smoke channel in orifice; right: new smoke channel in orifice.

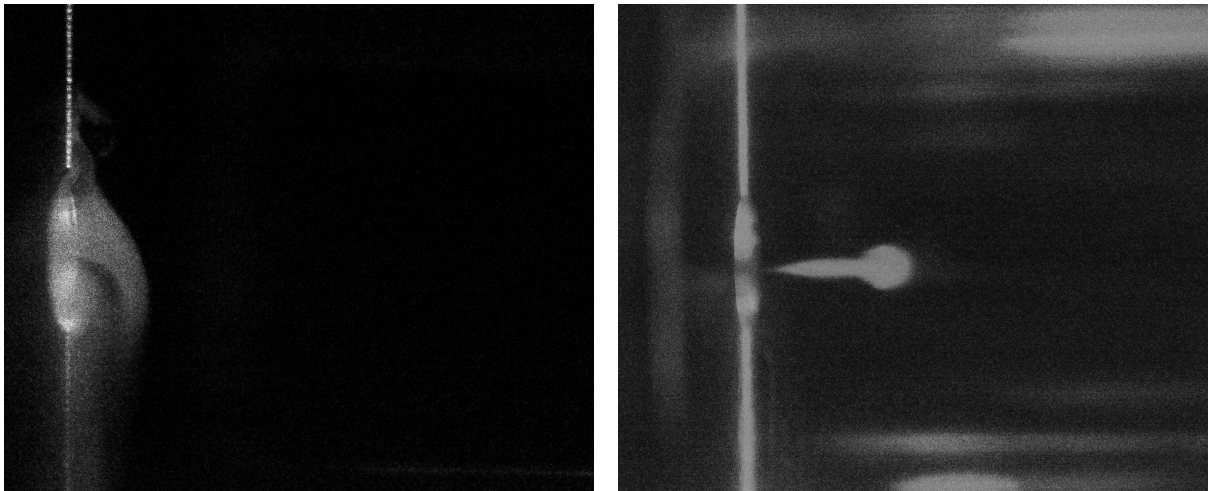


Figure 4.18: Left: smoke flow with existing smoke channel; right: smoke flow with new smoke channel; at 0.44 V with shutter speed 1/1000 sec, F/3.2 and ISO 25,600.

From this preliminary experiment it is clear that the hole on the side of the orifice works effectively. The only drawback is that the smoke is now ejected in one spot leading to vortices being seen in the direction that the smoke is inserted. When comparing the smoke flow with the new smoke channel with that of the existing smoke injection the new technique is clearly more focused on one point and does not create smoke that covers the whole area after the jet pump. Ideally, the smoke should enter the tube from all sides, suggesting a ring of some sort would be the best solution. This can easily be incorporated in the design of the jet pump as it will be 3D printed. The final design can be seen below in Figure 4.19, with a view of the jet pump as a whole in Figure 4.19a and a cross-sectional view where the smoke channel is clearly visible

in Figure 4.19b. It is desirable for the hole of the smoke injection to be as small as possible yet still allowing smoke to pass. The manufacturing company of the 3D-printed objects has a minimum diameter requirement of 4 mm [11]. The existing orifice set-up has a smoke injection of 3 mm which was sufficient for the smoke to easily pass through. Considering these factors the hole was chosen to have a diameter of 3 mm. The jet pump is placed in the center of a perspex tube of length 40.8 cm so that on either side at least 15 cm of space is left to visualize the flow.

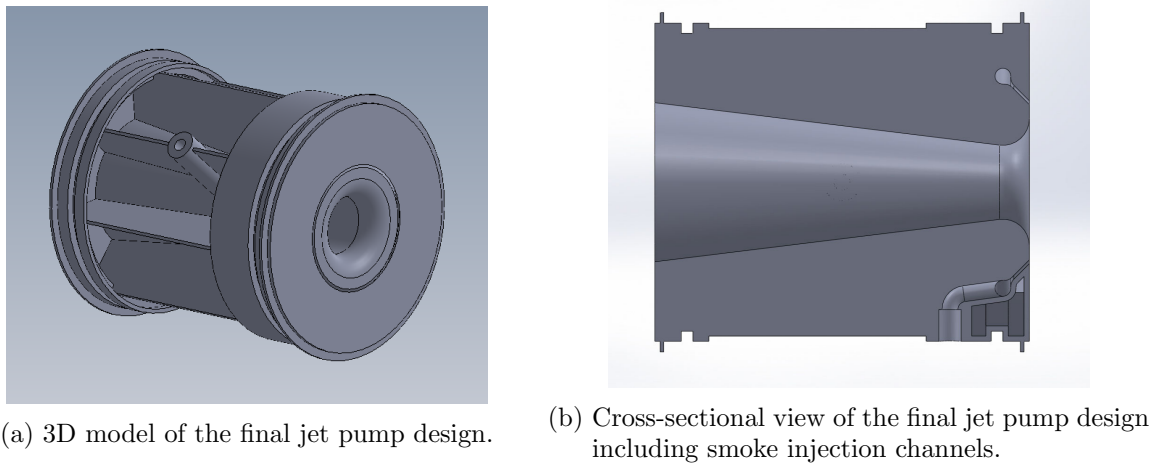


Figure 4.19: Final jet pump design viewed in its entirety and a cross-section of it.

### 4.3.2 Camera positioning and triggering

The camera is mounted so that its position can easily be adjusted while remaining at a  $90^\circ$  angle with respect to the laser sheet. When the camera is placed perpendicular to the laser sheet it is easier to bring the laser sheet into focus. A support is constructed such that the camera can move over three different axes: forward and backward, left and right, and up and down, shown in the photograph in Figure 4.20. The support is mounted on the rail of the set-up and it was observed during testing that the oscillations caused by the speaker did not result in any vibrations of the camera.



Figure 4.20: A sketch of the degrees of freedom of the camera and camera mount.

There are three settings on the camera which affect the exposure of the photographs: the aperture, the shutter speed and the ISO rating. These settings are essential to obtain bright and clear photographs with a limited light source. The camera is focused on the laser sheet and the aperture is kept at a maximum of  $F/3.2$  throughout the experiments to ensure that the most light falls onto the sensor. The shutter speed which is used for the experiments is  $1/1000$

seconds. At a frequency of 100 Hz this means that ten points in a period can be captured instead of the mean flow (one whole period in one image). The ISO value is kept at ISO 25,600 which is the maximum rating possible for the Nikon D5200.

For the triggering of the camera it is beneficial to do this externally to be able to create a circuit in which the exact timing of the picture is recorded. There is a certain delay between the time that the camera is triggered and the time that the actual picture is taken. By creating a circuit that measures the exact time that the picture is taken specific points of interest on the oscillating wave of the loudspeaker can be closely investigated and linked to the simulation data. This circuit is created based on the hot shoe (or flash shoe) on the camera as is shown in Figure 4.21. Where usually the flash fires at the instant that the photograph is taken, using the following circuit a signal is now sent to the labview software in the computer when the photograph is taken. Although due to the delay it remains impossible to take several photographs in one period, it is now possible to know at which point in time and thus at which position in one period the photograph was taken. Since the flow is assumed periodic, it is possible to visualize one period of the oscillation.

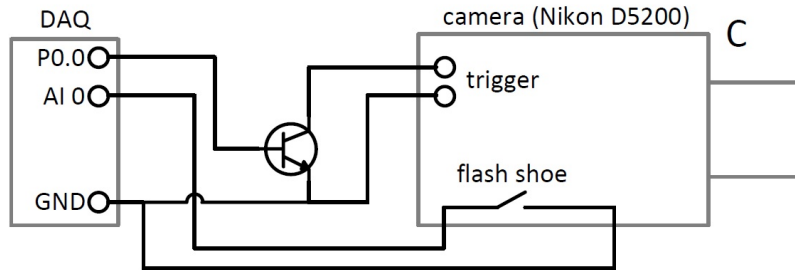


Figure 4.21: Camera triggering circuit.

### 4.3.3 Laser positioning

The 5mW laser used in the experimental set-up is positioned such that it can rotate  $360^\circ$  both vertically and horizontally and can be displaced over three axes, as can be seen in Figure 4.22. This ensures that the camera's required movements are limited while photographs can still be taken with the light sheet at various positions. It is beneficial to be able to rotate the light sheet because the optimum scattering off the smoke particles does not occur at a  $90^\circ$  angle. In the case of vanishingly small spheres ( $a \rightarrow 0$ ) the scattering of light has a maximum intensity in the forward direction ( $\Omega = 0^\circ$ ) and the backwards direction ( $\Omega = 180^\circ$ ). The minimum intensity occurs in the plane of symmetry, thus at an angle of  $90^\circ$ . As the radius of the sphere increases the *Mie effect* takes place, which is that more light is scattered in the forward direction than in the backwards direction [14]. It is expected that the *Mie effect* also occurs with the scattering of light from smoke particles; however, in order to make an approximation of this effect the average particle radius; the refractive index of the smoke particles and the refractive index of the surrounding medium have to be known. Although positioning the laser at a  $90^\circ$  angle does not provide the highest light intensity it is easier to focus the camera on the laser light sheet at this position.

The laser with mount is attached in the aluminum mount with a distance of 40 mm between the laser and the perspex tube and 28 mm to the left of the opening of the jet pump. With a fan angle of  $90^\circ$  this leads to a laser sheet with a width of approximately 90 mm at the center of the jet pump, sufficient for visualization of flow patterns.

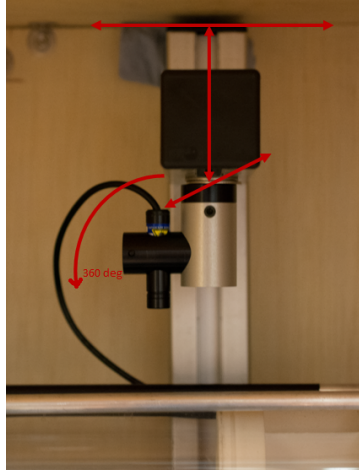


Figure 4.22: Degrees of freedom of the laser and laser mount.

#### 4.3.4 Camera box and smoke box

To be able to visualize the flow as effectively as possible it is essential that the smoke is illuminated exclusively by the laser light and that external light sources are eliminated. In order to do this a simple adaptation to the set-up is to place a box around the test section, the aluminum construction, the camera and the laser. In addition to eliminating external light sources the black box will act as an extra safety measure against the laser. The laser which is used, is a class 3 laser which entails that direct exposure can be harmful; however, since it is used as a line laser the intensity is less than the standard class 3 laser. Therefore, it is not considered harmful as long as direct exposure to the eyes is avoided. The box is constructed such that it can easily be opened in preparation for an experiment and it can be moved to a different section of the set-up if necessary. The box around the test section can be seen in Figure 4.23.

Along with the laser the smoke generator also requires alterations to the set-up for an optimum safety. The smoke generator runs on lamp oil whose fumes should not be inhaled as they contain alkanes. In addition an excess amount of smoke generation in the lab will cause the fire alarm to go off and can cause damage to the camera. A black air tight box is constructed around the smoke generator with an additional, larger, ventilator on one side and an outlet for the excess smoke on the other side. The excess smoke is filtered by a microfilter before entering the room and the ventilator enhances the effect of the ventilator on the smoke generator itself. Finally the box contains inlets for the power supplies, and an inlet for the lamp oil as well as an outlet for the smoke to pass into the jet pump. The design of the box around the smoke generator can be seen in Figure 4.24.

#### 4.3.5 High speed camera and laser recommendation

When visualizing the flow ideally one period is studied so that the flow structures in that period are observed. Previously this was done by using the Nikon D5200; however, the frame rate of 5fps limits the amount of pictures that can be taken per period. By using a high speed camera which has a much higher frame rate it is possible to take sufficient pictures in one period, thus avoiding the influence that the a-periodic flow may have on the accuracy of the study. In order to test the success of such a high speed camera preliminary experiments were performed using a Phantom v7.3 of Vision Research. This camera has a maximum frame rate of 6,688 fps at full resolution and can reach 500,000fps at a reduced resolution. A Nikkor 50mm Macro lens was mounted on the camera in order to improve the exposure settings. The exposure settings of the high speed camera set-up are: aperture of F/1.8, shutter speed of 1/1000 seconds, and an

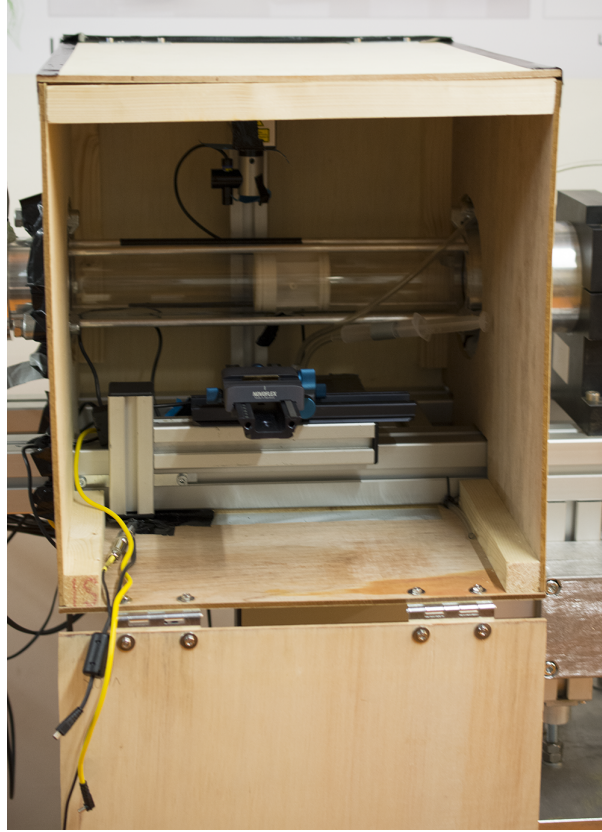


Figure 4.23: Box construction around the test section.

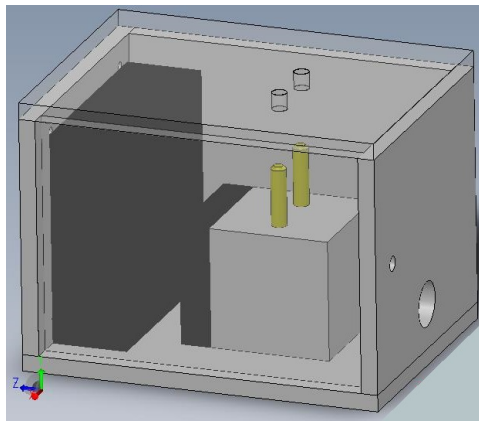


Figure 4.24: Box for around the smoke generator.

ISO rating of ISO 1,200 for color pictures. The results of the preliminary experiments clearly show that the light from the 5mW laser is insufficient to take clear photographs at the current settings. As almost nothing is visible on these photographs they were not included here. A comparison of the settings of the DSLR camera and the high speed camera indicates that a stronger laser would provide higher intensity light and thus clearer pictures. In Table 4.1 the important settings are compared in order to determine the minimum required strength of the laser. When considering the scaling factors between the different settings it can be concluded that a laser which is five times as strong will provide sufficient light.

A recommendation for optimizing the flow visualization is to use a high speed camera in order to study one period and to use a 60mW laser. The reason this was not applied in the current set-up

Camera	Required laser strength	Aperture	Shutter speed	ISO rating
Nikon D5200	5 mW	F/3.2	1/1000	25,600
Phantom v7.3	60 mW	F/1.8	1/1000	1,200

Table 4.1: Camera settings of high speed camera and digital camera compared

is due to the safety requirements accompanied with installing such a laser. Since it is a class 3 laser the lab would need to be fitted with laser warning systems and this would require several months before completion. The specific laser which is recommended is a 60mW green laser line. A green laser will result in sharper images than a red laser due to the functioning of a digital camera. A digital camera uses millions of tiny light cavities to record an image, a filter is placed over these cavities to capture one of each of the three primary colors in each. The Bayer array, which is the most common, contains twice as many green pixels as red or blue, as can be seen in Figure 4.25. As a result the use of a green laser light will lead to an image with less noise [10].

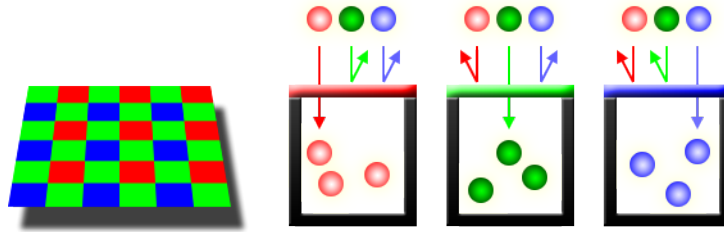


Figure 4.25: Digital camera sensor, Bayer array [10].

# 5 Experiments and results

## 5.1 Pressure measurements

In the following section the various pressure measurements with the jet pump are presented and discussed in comparison to the analytical model described in Section 3.3 and the CFD simulation results. In order to be able to compare these results, it is necessary to present the pressure measurements as a function of the velocity in the jet pump. The pressure measurements are first presented as a function of the far field pressure amplitude in the set-up and subsequently as a function of the flow rate.

### 5.1.1 Time-averaged pressure drop measurements

To determine the effect of the jet pump it is of interest to perform various pressure sweeps using three different terminations of the set-up. A closed end produces a standing wave as the sound wave is completely reflected. An open end ensures that the incoming wave and reflected wave are out of phase by 180 degrees. The resonator termination is almost a perfect absorber, with a reflection coefficient of almost zero, and causes a traveling wave to be formed. For each of these terminations, the time-averaged pressure drop over the set-up is measured against the far field pressure amplitude. The pressure amplitude measured by pressure sensor P4 is taken as the far field pressure amplitude as it is the closest to the loudspeaker. The sketch in Figure 5.1 shows the positioning of the sensors and the manometer that is used for the following experiments.

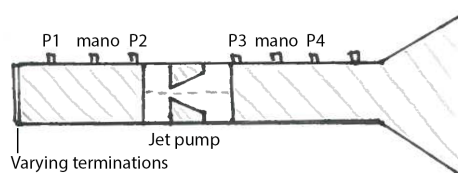


Figure 5.1: Sketch of the positioning of the manometer and pressure sensors for the following tests.

For the three tests, the loudspeaker audio volume was increased every two minutes while the reading on the manometer was noted every minute as a check. The same maximum audio volume is used for all the experiments and the set-up is run at a frequency of 113 Hz so that minimum reflection occurs when the resonator termination is attached. In order to check whether the resonator is indeed creating a traveling wave, the phase difference between the two sensors on the left hand side of the jet pump (P1 and P2) are compared for the resonator case and the closed end case, shown in Figure 5.2, prior to performing the pressure measurements. Only the phase differences are compared to the left of the jet pump because on the right-hand side there is reflection from the jet pump, providing uncertainty in the wave which is formed in this section.

In Figure 5.2 it can be seen that the phase difference between P2 and P1 in the closed set-up is smaller than the phase difference between P2 and P1 in the set-up with the resonator end. The phase difference in the closed set-up remains constant at a value of around 0.4 deg. This is in accordance with the fact that in the closed set-up a purely standing wave is formed and thus over time there should not be a change in the phase difference. The phase difference between P2 and P1 changes over time which is expected as a purely traveling wave is formed. It is

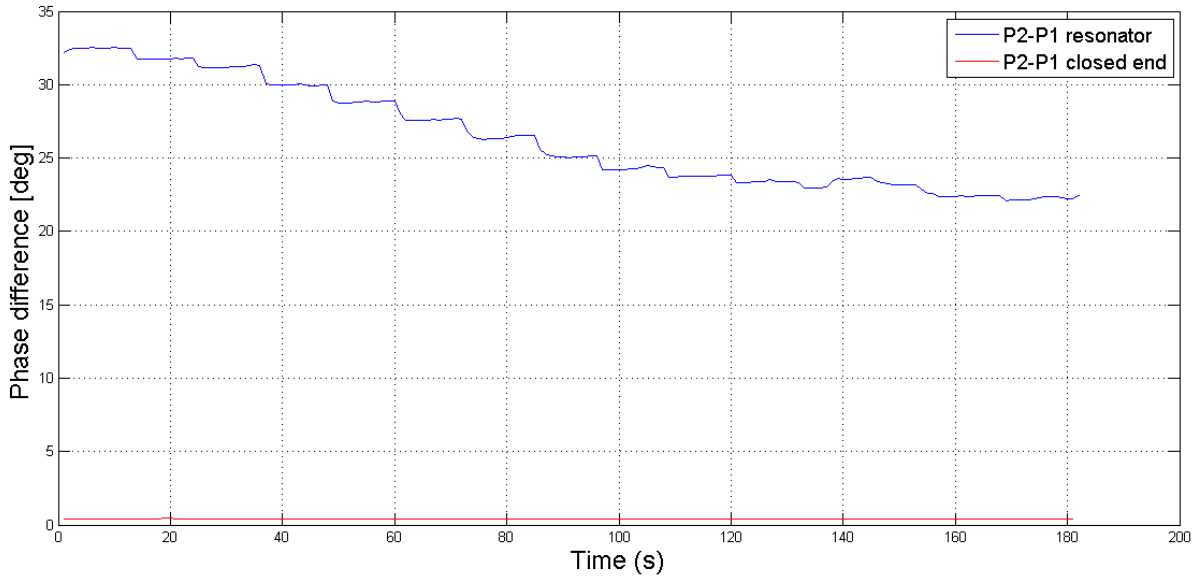


Figure 5.2: The phase difference between P1 and P2 and the difference between P3 and P4 for closed end and resonator termination.

concluded that the resonator termination is performing as it should and is indeed creating a traveling wave in the set-up.

Using the same conditions as described for the phase difference test, the pressure measurements are carried out. Figure 5.3 shows the combined results of the time-averaged pressure drop over the jet pump against the far field pressure amplitude for the three terminations. For clarity this plot only displays the time-average pressure drop measured by the difference between the mean pressure at sensor P3 and that at P2, the two sensors which are closest to the jet pump on either side.

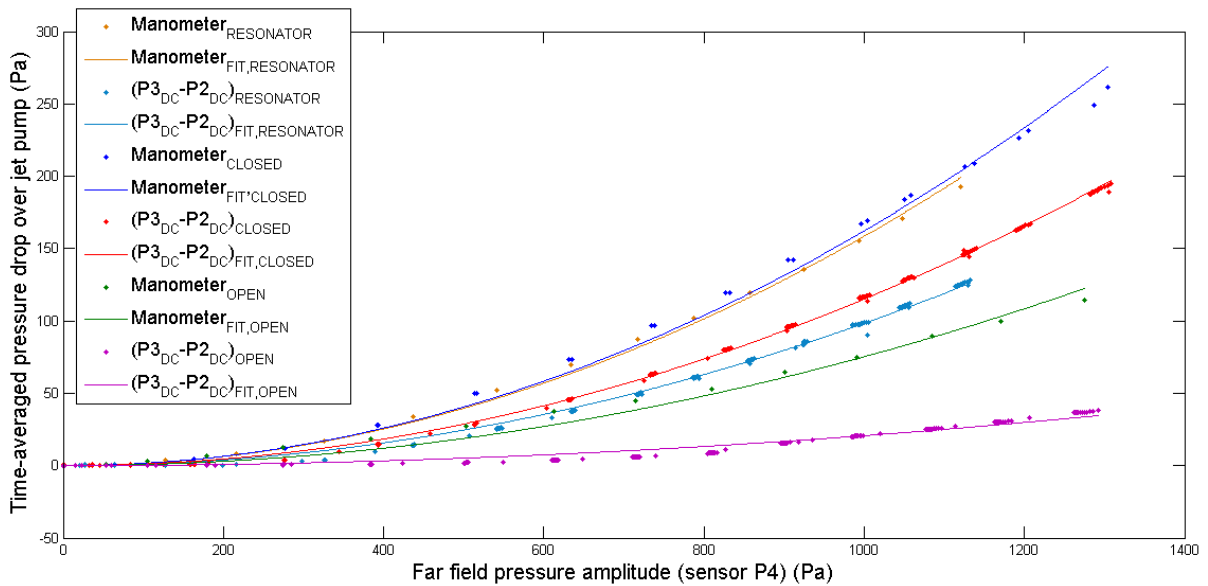


Figure 5.3: Time-averaged pressure drop over the jet pump against far field pressure amplitude for three different terminations.

The points are all fitted with a purely quadratic curve of the form  $y = ax^2$ . Based on Equation (3.10) it is predicted that the time-averaged pressure drop will increase quadratically with the velocity in the jet pump. Since the velocity in the jet pump is proportional to the far field pressure amplitude, as will be elaborated on in the following section, the relationship between the far field pressure amplitude and the time-averaged pressure drop is also purely quadratic.

From Figure 5.3 it is observed that the manometer readings differ significantly from the pressure drop measured by the pressure sensors, especially at high pressure amplitudes. In addition, the curves of the results measured by the pressure sensors display a better quadratic relationship as the curves fit through the points more precisely. This reinforces the accuracy of the pressure sensors over the differential pressure gauges. The termination which results in the highest time-averaged pressure drop over the jet pump is the closed end, the open end giving the lowest, and the resonator termination giving values between these two. In order to compare these experimental results with the CFD simulations as well as the analytical model, it is necessary to plot the time-averaged pressure drop against the velocity in the jet pump.

### 5.1.2 Comparison with analytical model and simulations

In order to compare the experimental results with the analytic model which is described in Chapter 3 and the simulation results described in Section 3.4, the velocity in the jet pump needs to be determined. As an initial estimate results of available simulations made in the Acoustics Module in COMSOL Multiphysics v4.4 are used. These available simulations are an acoustic simulation of the set-up, including the jet pump, with three different terminations: an open end, a closed end and the resonator termination. The velocity amplitude in the jet pump is compared to the pressure amplitude at the location of sensor P4, shown in Figure 5.4.

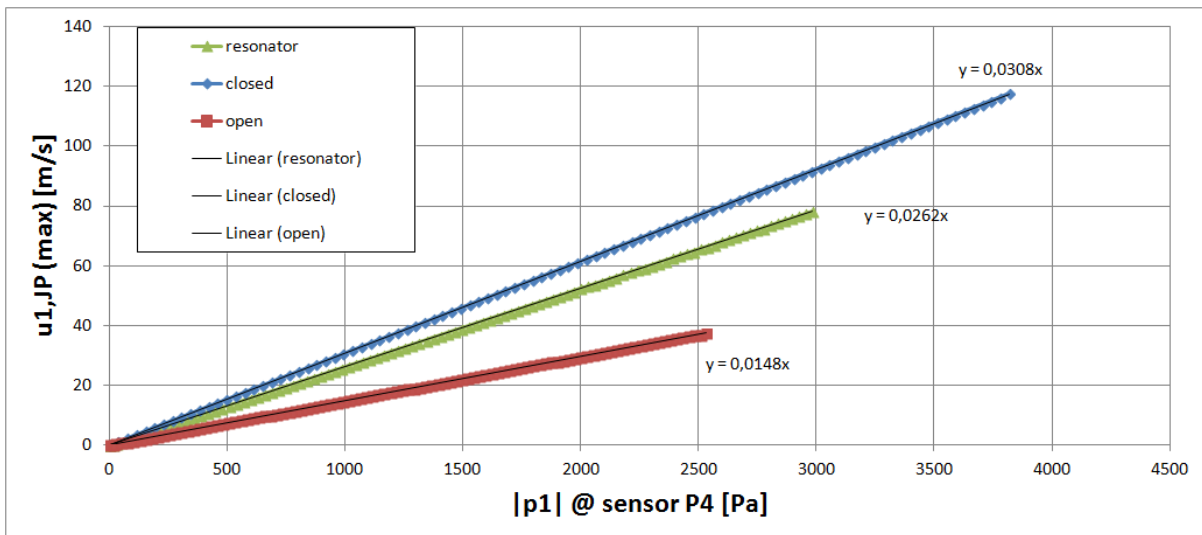


Figure 5.4: Relation between the velocity in the jet pump and the pressure amplitude at sensor P4.

The curve in Figure 5.4 illustrates a linear relationship between the velocity amplitude in the jet pump and the pressure amplitude at sensor P4. The relationship of the velocity amplitude over the pressure amplitude is a measure of the resistance of a jet pump. Using this model it is assumed that the impedance, which is the resistance over the average velocity amplitude, is linear. However, Petculescu [1] and Ingård and Labate [21] both found that especially at low pressure amplitudes this is not the case. That is why this remains an initial estimate. The slope

of the curve for each of the three terminations is used to translate the pressure amplitudes measured at sensor P4 during experiments into a velocity in the jet pump. Using this translation it becomes possible to present the experimental results in terms of the time-averaged pressure drop against the velocity in the jet pump, which is necessary for the desired comparisons. The comparison of the analytic model, the simulated model, and the experimental results is shown in Figure 5.5.

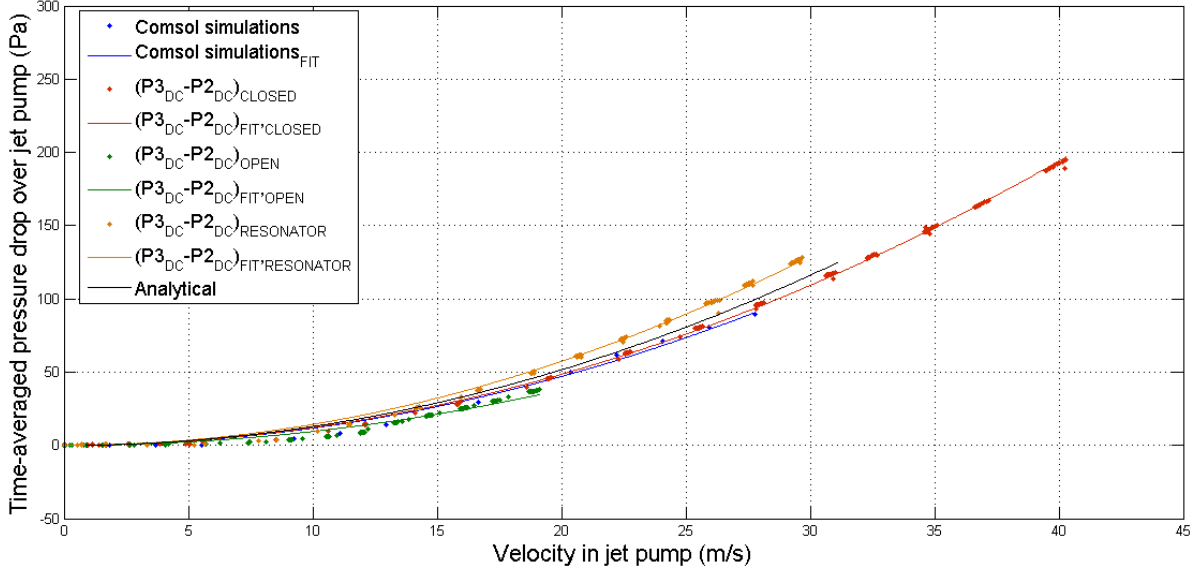


Figure 5.5: Time-averaged pressure drop over the velocity in the jet pump for three terminations, simulations and analytical model.

The first thing which is immediately observed from this plot is that the time-averaged pressure drops are all in the same order of magnitude. This is a very positive result as it illustrates that the analytic model and the simulated model both present realistic values. To compare the specific curves, it is essential to note that the simulation was performed using an open ended resonator tube.

From Figure 5.5 it is clear that these expectations are not fulfilled entirely. However, the maximum deviation is in both cases approximately 10 Pa. Possible explanations of this deviation is that for the open end the COMSOL simulation assumes a reflection coefficient of exactly -1, while that cannot realistically be achieved during experiments. There will always be reflections from objects in the environment as well as from the edges of the tube. The COMSOL model also simulates a flow which is incompressible and isothermal, however, these are assumptions which cannot be achieved in reality. Without the jet pump in the set-up the resonator termination has a reflection coefficient of 0.04 which is very close to the “ideal” value of zero. The reflection coefficient could not be measured quantitatively once the jet pump was inserted due to the extra reflections caused by the jet pump. In addition, as was explained earlier, the acoustic simulation that is used to determine the velocity in the jet pump for the three different situations is only a first estimation and is not expected to return completely realistic values of the velocity amplitude since the impedance is not linear.

Considering the various assumptions and differences in the experimental set-up and the models made by both the simulations and the analytical results, the curves in Figure 5.5 fulfill the expectations. The fact that the analytical model is in close accordance with the experimental results for the resonator termination also says something about the assumptions which were made when

creating the model. One of these assumptions, which is still the subject of ongoing study in the field of thermoacoustics, is that the minor loss coefficients have the same values in oscillatory flow as they do in steady flow. The minor loss coefficients which are calculated in the analytical model, based on the geometry of the jet pump as described in section 3.3, are:  $K_{con,s} = 0.04$ ,  $K_{con,b} = 0.5$ ,  $K_{exp,s} = 0.8941$ , and  $K_{exp,b} = 0.5625$ . Based on the correspondence between the analytical model and the experimental results it can be concluded that for the current geometry, these minor loss coefficients, although defined for steady flow, also hold for oscillatory flow.

## 5.2 Flow visualization

### 5.2.1 Description of observed flow structures

One of the main goals of this assignment is to obtain a qualitative image of the flow field, with the presence of the jet pump, at several instances in time and thus positions on the acoustic wave. To do this the camera, smoke generator, and laser are set up as described in Section 4.3 and the camera triggering device is connected to the computer. All these features can be controlled externally so that the box around the area of testing is closed off to ensure no external light enters the set-up. Following initial experimentation to optimize the working of the flow visualization set-up, a range of tests are done at varying pressure amplitudes. All the photographs which are presented in this section are taken at a shutter time of 1/1000 second, an aperture of F/3.2 and an ISO rating of 25,600. The laser is positioned perpendicular to the camera and the jet pump is at the right-hand side of the photographs with the speaker positioned to the right of the jet pump, as shown in the sketch in Figure 5.6. The set-up is run at 113 Hz for all the following tests to optimize the working of the resonator termination.

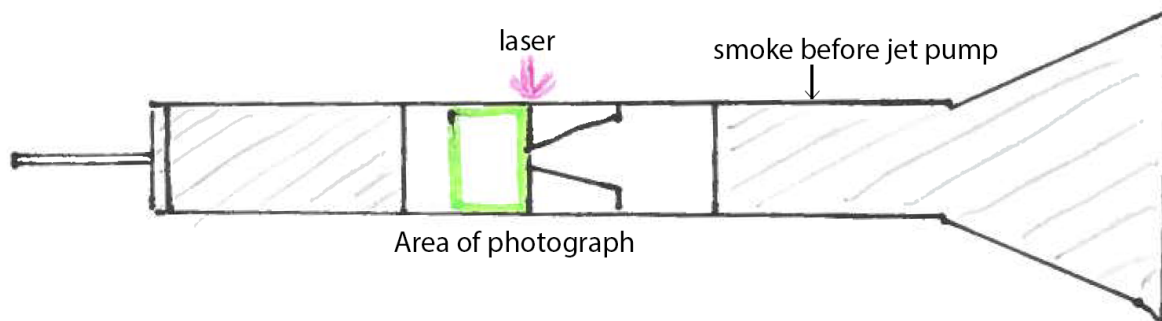


Figure 5.6: Sketch of the set-up for flow visualization as viewed from the camera, where the green square represents the area of the photographs, the purple arrow the positioning of the laser, and the position of smoke injection before the jet pump is also indicated.

At each pressure amplitude a series of approximately 100 photographs are taken successively, in order to visualize one period of the acoustic wave. Theoretically, the flow is periodic and it is expected that when the photographs are grouped per phase, and thus per position on the acoustic wave, they will display similarities per phase. Since the photographs are taken with a shutter time of 1/1000 seconds, at the frequency of 113 Hz this means that each photograph captures approximately one tenth of a period. It is thus chosen to cut the period into eight sections, each with a range of  $45^\circ$ , and the photographs are placed in one of these sections depending on their phase. This results in the study of the flow at various pressure amplitudes at eight positions in a period. These results can be viewed in Appendix 8.2 for a pressure amplitude of 40 Pa, 60 Pa and 80 Pa.

According to the theory, each of the photographs in one row, which represents one phase section, should display identical patterns in the flow. This trend is, however, not observed in the results of the flow visualization tests as significant differences are present between the photographs in the same row. From this it can be concluded that the flow is not periodic or that the smoke injection has too much influence on the flow patterns formed. During these tests the smoke was turned off after approximately twenty photographs were taken to ensure that there is not too much smoke built up in the set-up.

The effect of turning off the smoke generator and the fan of the smoke generator are determined by performing an additional test. First the smoke is inserted into the set-up with everything turned off, next the loudspeaker is turned on, then the smoke generator is turned off; and finally the fan of the smoke generator is turned off. Images of this process are shown in Figure 5.7. The smoke falls to the bottom of the tube when the set-up is not turned on and vortices start to form immediately after turning the loudspeaker on. Once the smoke and the fan of the smoke generator are turned off similar vortices are still viewed, eliminating the influence of these factors on the flow patterns. The vortices do become less clear once the smoke is turned off and to test the influence of the smoke injection another test is performed where the smoke is inserted before the jet pump, as shown in Figure 5.6. The smoke already starts to move through the jet pump prior to turning on the loudspeaker and once the acoustic wave starts, similar flow patterns as those observed in the previous test are displayed, as shown in Appendix 8.3. The main conclusion is that the same flow patterns are observed independent of the position of smoke injection and the fan of the smoke generator. For further analysis, instead of comparing the photographs grouped per phase, specific images are chosen per pressure amplitude to highlight certain flow features which are observed.

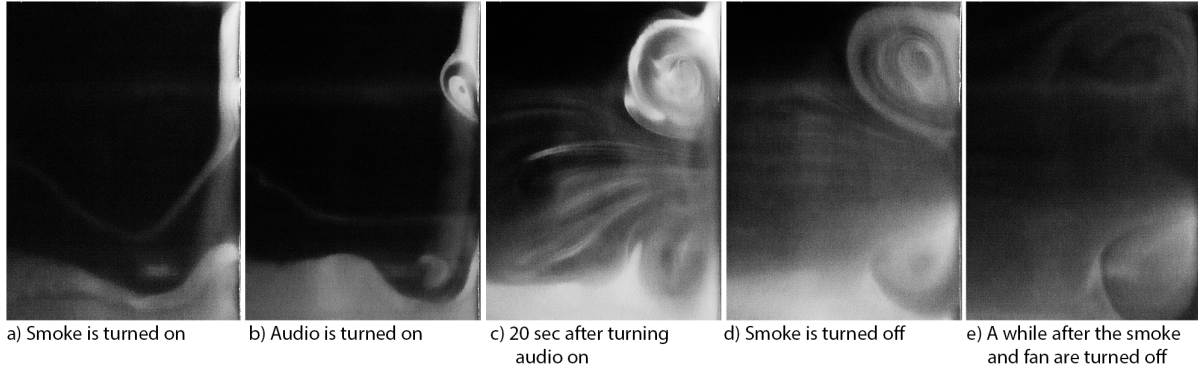
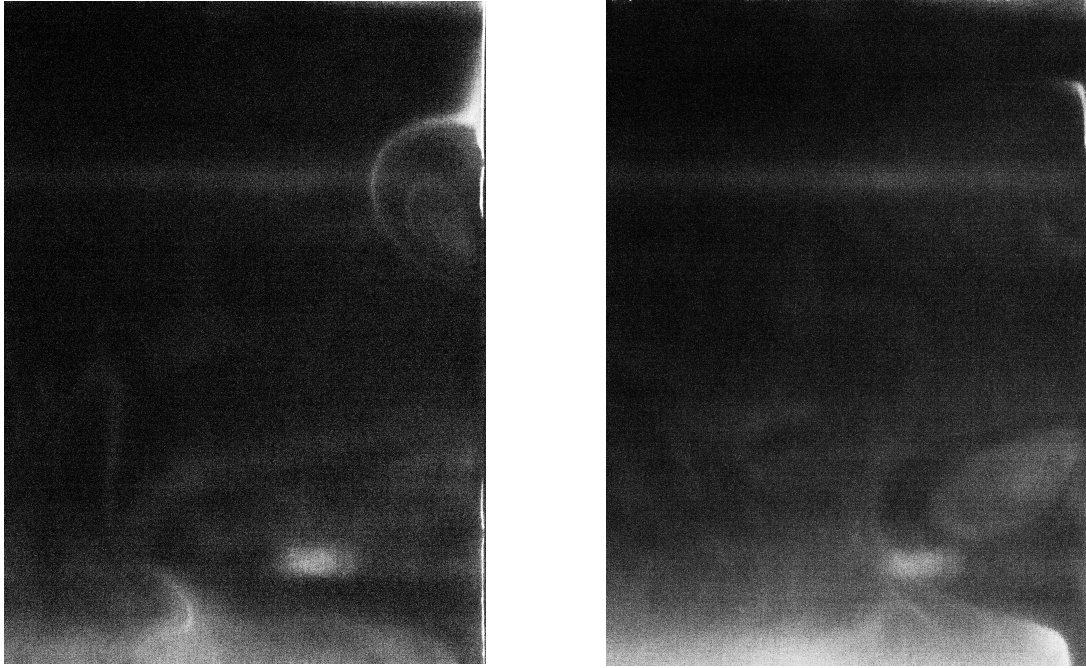


Figure 5.7: Process of injecting the smoke into the set-up where the images show the flow at different stages.

At pressure amplitudes below 25 Pa there are no vortices observed in the flow and generally no specific flow patterns can be distinguished. At 25 Pa two tests are done at the same settings, resulting in two different flow patterns observed, as seen in Figure 5.8. In Figure 5.8a a vortex starts to form at the top right-hand corner of the image while in Figure 5.8b a vortex is formed at the bottom right-hand corner. In both cases it seems that the smoke is not sufficient or that the amplitude is not high enough to cause significant disturbances in the smoke.

At a pressure amplitude of 40 Pa flow structures are more clearly visualized in the images seen in Figure 5.9. Shortly after the smoke is turned on, which is illustrated in Figure 5.9a, it is seen that the smoke tends to drop towards the bottom of the tube. At the top the acoustic flow causes the smoke to circulate in an anticlockwise direction while the smoke is being pulled down due to gravity. The anticlockwise circulation, where the flow is going towards the jet pump, is



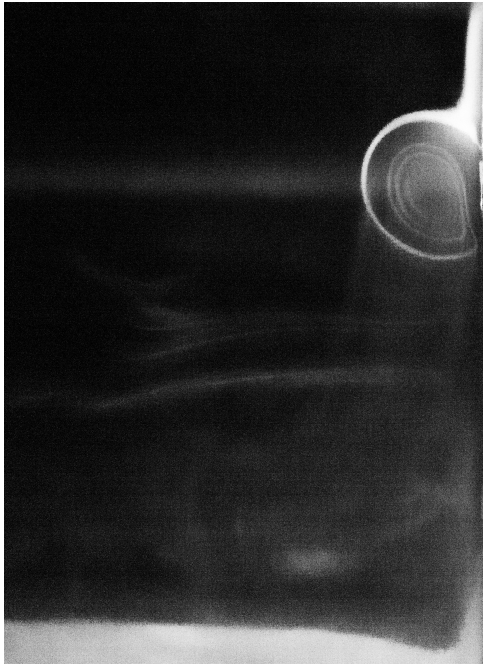
(a) First test at a pressure amplitude of 25 Pa. (b) Second test at a pressure amplitude of 25 Pa.

Figure 5.8: Flow visualization at a pressure amplitude of 25 Pa, camera settings: ISO 25,600, F/3.2. and shutter time 1/1000 sec.

identified by the spacing between the smoke flow. At the bottom inlet the smoke falls to the bottom of the tube along the edge of the jet pump, and thus not experiencing any effects by the acoustic flow. As the smoke builds up in the set-up, the vortices display more symmetric qualities, as is seen in Figure 5.9b. Two symmetric vortices with a flow into the jet pump can be seen at the top and bottom. From this image it is difficult to distinguish what is happening in the center of the jet pump. However, during the experiments it could be seen that there was a mean outflow from the jet pump.

At higher pressure amplitudes the in- and outflow of the smoke flow from the jet pump can be seen more clearly. At a pressure amplitude of 60 Pa a similar trend is seen as in the images at 40 Pa as only after approximately 16 seconds the vortices at the bottom of the jet pump become visible. Figure 5.10a shows the flow patterns observed once enough smoke is built up in the set-up. From this image two symmetric vortices are clearly seen to be circulating with a flow into the jet pump. The darker rounded region in the center of the jet pump illustrates the outflow from the jet pump, which was also observed during the experiments. The streams of smoke in the center of the image is the smoke which flows into the jet pump. These observations compare to the transition region described by Ingård and Labate [21]. That is, the transition between region 1, where only outflow is observed, and region 2, where only inflow is observed, with this transition region shown in Figure 5.10b. Although these regions are described for the flow through an orifice, similar flow patterns are observed for the flow through a jet pump. The orifice in Figure 5.10b is on the left-hand side of the image.

At higher pressure amplitudes it becomes difficult to capture the flow as mixing is too high and the amount of images which can be taken per second is too low. At a pressure amplitude of 100 Pa the flow patterns in Figure 5.11 are observed. The two symmetric vortices can still be distinguished as flowing into the jet pump while in the center there is only a strong flow into the jet pump as the smoke is being sucked in. At higher amplitudes the smoke in the set-up

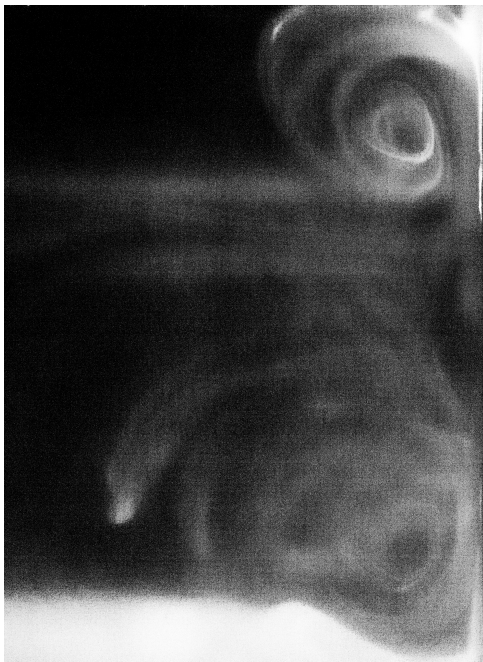


(a) Flow patterns at 40 Pa at  $t = 36$ s.

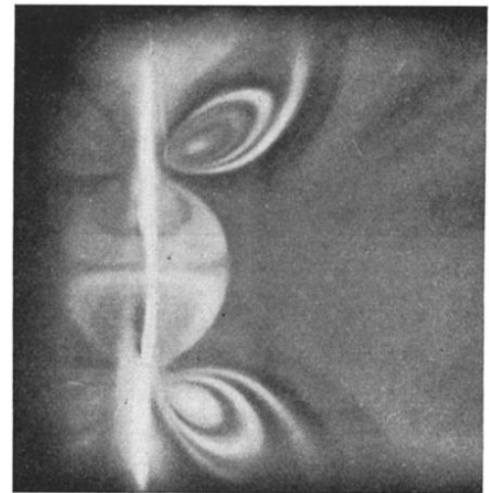


(b) Flow patterns at 40 Pa at  $t = 78$ s.

Figure 5.9: Flow visualization at a pressure amplitude of 40 Pa, camera settings: ISO 25,600, F/3.2. and shutter time 1/1000 sec.



(a) Flow patterns at 60 Pa at  $t = 35$ s.



(b) Flow patterns observed by Ingård and Labate [21] of the transition between region 1 and 2.

Figure 5.10: Flow visualization at a pressure amplitude of 60 Pa, camera settings: ISO 25,600, F/3.2. and shutter time 1/1000 sec and results of Ingård and Labate[21] as a comparison.

either builds up too much to be able to visualize anything if the smoke generator was left on, or the smoke disappeared too quickly for visualization when the smoke generator was turned off.



Figure 5.11: Flow patterns at a pressure amplitude of 100 Pa.

Although some flow patterns can clearly be observed in the photographs produced during this set of flow visualization experiments the desired result was not achieved. There were no vortices visualized which traveled through the tube and there were no jets observed. It was not possible to visualize the flow at pressure amplitudes higher than 100 Pa which is possibly when these effects appear. Being able to take more photographs in a shorter period of time could also result in the visualization of these effects. The smoke also seems to have too much influence on the flow patterns observed, not by the method of injection but because the amount of smoke in the set-up highly influences what is visible in the images. These factors negatively influenced the effectiveness of the visualization of the flow in one period of the acoustic wave, as described at the beginning of this section. The various problems encountered during flow visualization will be addressed and recommendations will be made in Chapter 6.

## 6 Discussion and Recommendations

Throughout the experimentation during this study, various problems with the set-up were brought to light and ideas for future tests were constructed. The visualization of the flow through the set-up provided the most set backs and also did not provide very good results. There are certain ways in which the current set-up can still be improved for the smoke visualization. However, a new technique for the visualization is also considered and should be studied in more detail. Flow visualization can also be used to study the various methods of measuring the pressure and to determine whether certain devices influence the flow in the set-up. Finally, there is a lot of room to continue with this study by designing different jet pump geometries and performing tests with these. In this section these three elements are elaborated on.

### 6.0.2 Pressure measurements

The pressure measurements performed in Section 4.2 and Section 5.1 present certain elements which could be improved in future experiments. The study of the effect of the presence of the differential pressure gauge on the pressure measurements was studied in Section 4.2. The results indicate that the pressure gauge does not significantly effect the pressure readings. However, the readings between the pressure gauge and the digital pressure sensors do differ significantly. Although the reason for this is described it is desirable to determine if there is indeed significant streaming present around the inlet of the pressure gauge in the set-up. This could be done by the use of the flow visualization technique of adding smoke into the set-up and illuminating a smoke sheet. The jet pump would need to be removed and a tightly shut entrance would need to be made in the perspex tube where the pressure gauge could be attached. The study of the flow around the inlet would not only be of interest for the pressure gauge but also for the digital pressure sensors and the needle valve. It can then be said with certainty what the actual effect is on the flow of inserting one of those three elements.

The needle valve which was used in order to control the mean pressure build up in the set-up also provided some problems. The main disadvantage of the needle valve was that it did not allow a significant amount of flow to pass through unless it was completely open. There was not a significant difference observed when opening the valve by one cycle of rotation each time, indicating that very little flow was allowed to pass through. It is suggested to look for a better needle valve. If, however, the visualization of the flow around the needle valve shows that it does not have any effect on the flow and there are no streaming effects around the inlet it is advisable to use this needle valve when it is completely open. It was presented in Section 4.2 that when the valve is opened completely, it leads to a zero mean pressure build up in the set-up. This is beneficial also for the smoke flow visualization as the smoke will no longer build up in the set-up and thus a more constant injection of smoke can be achieved.

### 6.0.3 Flow visualization

The results of the flow visualization experiments presented in section 5.2 indicate that there is still room for improvement of this technique. There remain a lot of disadvantages to using smoke with the main problem being that the smoke seems to significantly influence the flow patterns which are observed. The smoke is now inserted directly into the flow while ideally the flow would take the smoke with it and thus visualizing the path that the flow takes. A method to do this would be to insert the smoke before the jet pump when the acoustic set-up is turned

off. As the loudspeaker is turned on the flow will pass through the smoke, taking smoke particles with it to create the visualization. This concept was tested by inserting the smoke through one of the holes on top of the set-up, designed for pressure measurements. The result was not very different from inserting the smoke directly into the flow as the smoke already started moving through the jet pump while the acoustic set-up was switched off.

In order to reduce the influence of the smoke a continuous method of injecting the smoke must be developed. Currently the smoke is inserted at the start of the experiments and, in order to ensure that not too much smoke is built up in the set-up, is turned off again after approximately one minute. This results in photographs where the flow features may only be a result of the amount of smoke which was present in the set-up. It is difficult to control this smoke injection as the smoke generator cannot be regulated very easily and the mean pressure build up in the set-up will always result in the smoke building up. If the needle valve is found to have little effect on the flow, this could solve the problem and otherwise it is desirable to look into another technique for flow visualization.

The technique which has the greatest potential in creating the best photographs for this set-up is the shadowgraph technique also used by Smith and Swift [3]. This technique was also considered and investigated in previous studies of flow visualization for this set-up. However, it was concluded that it would not be effective as the necessary density gradient in the flow caused by acoustic waves is too small [20]. The technique that Smith used to overcome this problem was to add a small amount of hydrofluorocarbon R134a into the flow [3]. The effect of this hydrofluorocarbon on the acoustic equipment would need to be investigated. It is possible that the same problems with the smoke is observed, as the gas may sink to the bottom and build up in the set-up. A necessary alteration to the set-up would be that a good filtering system would need to be created in order to ensure that none of the hydrofluorocarbon is released into the atmosphere.

The shadowgraph technique only requires a spherical mirror or lens that will create a parallel light beam and another lens to focus the light rays which pass through the flow field onto a recording plane, shown in Figure 6.1. The technique is based on the fact that changes in the density of a fluid lead to differences in refractive index. When light is thus passed through such a fluid the individual light rays are refracted and will deviate from their original path. The light intensity which is then observed on the recording plane is altered with respect to the undisturbed case [6]. Essential to this technique is thus that there are significant density differences in the fluid, which can be enhanced by the addition of hydrofluorocarbon R134a. There will be some alterations to the set-up required if this technique is to be used for the flow visualization, however, it has the potential of creating better photographs than the smoke injection.

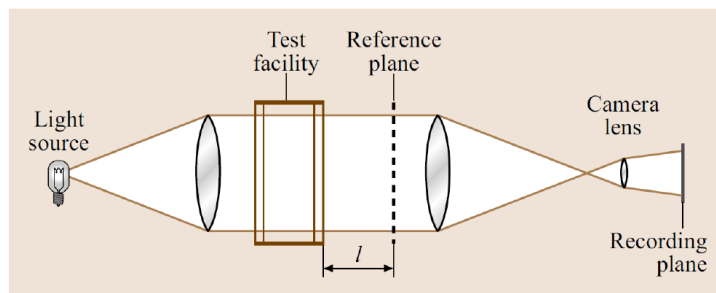


Figure 6.1: Shadowgraph technique used for flow visualization [6].

An improvement for flow visualization which has already been discussed in Section 4.3 is the

use of a high speed camera to take photographs and the use of a more powerful laser. The advantages of using a high speed camera is that more frames per second can be captured, making it possible to study one whole period of the acoustic wave. It is clear from the flow visualization results that the acoustic wave is not purely periodic, thus making it difficult to merge the photographs taken over various periods. If a high speed camera is to be used to capture the flow it is also necessary to use a different laser source if the smoke injection technique is to be used. The 5mW laser does not provide enough light for the settings of the high speed camera and thus it is suggested to buy a 60 mW green line laser. As this is a class 3 laser this will require extra safety measures to be taken in the laboratory so that exposure to the laser is avoided at all times. If, however, the shadowgraph technique is to be used the light source does not have to be a laser and instead even a powerful lamp could be used. The installation of the high speed camera would require some alterations to the set-up as it is too large to fit in the box which is now constructed around the set-up. Another method to fix the camera on the set-up would also have to be designed as the camera is rather large, heavy, and very costly. Although using the high speed camera required too many alterations to the set-up to install it in the limited amount of time, it will provide insight into the flow patterns which is of great interest.

The last simple alteration to the set-up which will improve the flow visualization is removing all unwanted reflections in the set-up. The construction of the box around the section of the set-up where the flow visualization takes place is already a good improvement. However, there are still unwanted reflections caused by the equipment in the box. The perspex tube itself and the aluminum tubes which are used to hold the construction in place provide the most reflections. It is advisable to spray the inside of the perspex tube black, leaving a window for the smoke visualization as well as one for the light source. The aluminum tubes of the construction should all be painted black and the jet pump itself should also be painted black as this also caused light from the laser sheet to be reflected.

#### 6.0.4 Jet pump design

During this study a single jet pump was designed and tested with a specific geometry as an initial trial. It is, however, desirable to study the flow patterns and to perform pressure measurements over a range of geometries. The effect of the taper angle as well as the size of the jet pump are both factors which are interesting for further studies. The taper angle of the jet pump was varied in the tests performed by Petculescu and Wilen [1] and from their conclusions we also made the choice of using a taper angle of  $7^\circ$ . It may, however, be of interest to vary the taper angle and subsequently compare the results with those of Petculescu.

In this study experimentation is done using one large jet pump which fits precisely in the set-up. It is of course also possible to create a structure, that can be inserted in the set-up, containing several smaller jet pumps. Various factors come into play for this design including the size of the individual jet pumps; the spacing between them; the arrangement of them; and the amount of jet pumps in one structure. All of the jet pumps can be designed with the same geometry or different geometries can be incorporated into one structure. These are all things which need to be studied in depth and provides a whole set of new possibilities in this field of research.

The smoke injection is something that still causes a lot of problems in the visualization of the flow. It was not desirable to create an inlet for smoke injection inside the jet pump because this would influence the pressure measurements. It would, however, be an option to 3D print a jet pump with the same geometry as the jet pump which was designed in this bachelor assignment with a new smoke injection method. The pressure measurements have already been performed for that geometry and considering the accuracy of the 3D printing the jet pumps can be assumed

## CHAPTER 6. DISCUSSION AND RECOMMENDATIONS

identical. The smoke could then be injected inside the jet pump so that the pressure causes the smoke to be pushed through, perhaps having less influence on the flow.

## 7 Conclusion

Two different sets of experiments were performed with the jet pump that was designed based on an analytical model: pressure measurements and flow visualization experiments. The results of the pressure measurements were analyzed and compared with the analytical model as well as a simulated model. The models showed a clear match with the experimental results. The agreement between the analytical model and the experimental results strengthens, for this geometry, the assumption made that the minor loss coefficients have the same values in oscillatory flow as they do in steady flow. However, these results remain an initial estimation.

To obtain qualitative images of the flow field of the acoustic wave at several instances in time the existing technique of smoke flow visualization [20] was extended and optimized. The main features which were altered were the camera triggering and the method of smoke injection. Various images were captured at a range of pressure amplitudes displaying clear flow patterns. However, the technique of smoke flow visualization remains problematic and a clear image of the flow field of one period of the acoustic wave was not obtained. It is concluded that another technique for flow visualization should be investigated as the smoke seems to have too much influence on the flow.

# Bibliography

- [1] A. Petculescu and L. A. Wilen, “Oscillatory flow in jet pumps: Nonlinear effects and minor losses”. Department of Physics and Astronomy, Ohio University, Athens, December 2002.
- [2] B.L. Smith and G.W. Swift, “Measuring second-order time-average pressure”. Condensed Matter and Thermal Physics Group, Los Alamos, New Mexico, 2001.
- [3] B.L. Smith and G.W. Swift, “Power dissipation and time-averaged pressure in oscillating flow through a sudden area change”. Acoustical Society of America, 2003.
- [4] B.S. Massey and J. Ward-Smith, “Mechanics of Fluids”. Seventh Edition, Volume 1. CRC Press, 1998.
- [5] C.E. Kindsvater, “Energy Losses Associated With Abrupt Enlargements in Pipes”. River Hydraulics, Washington, 1961.
- [6] C. Tropea, A. L. Yarin, and J. F. Foss, Eds., Springer Handbook of Experimental Fluid Mechanics. Berlin, Heidelberg: Springer Berlin Heidelberg, 2007.
- [7] C. Veret, “Flow visualization by light sheet. Flow Visualization III: Proceedings of the Third International Symposium on Flow Visualization, W. Yang, Ed. 1985, pp. 106112.
- [8] D. van der Gun, “Design and Realization of an Experimental Thermoacoustic Setup”. Master thesis, Laboratory of Thermal Engineering, University of Twente, 2013.
- [9] D.J. Szarko, “Smoke-wire visualization of an oscillating flow in a gas spring. Massachusetts Institute of Technology, 1993.
- [10] “Digital Camera Sensors.” Understanding Digital Camera Sensors. Cambridge in Colour, n.d. Web. 29 Apr. 2014. <<http://www.cambridgeincolour.com/tutorials/camera-sensors.htm>>.
- [11] “Frosted (Ultra) Detail Plastic 3D Printing Material Information - Shapeways.” Shapeways. Shapeways Inc., n.d. Web. 3 May 2014. <<http://www.shapeways.com/materials/frosted-detail-plastic>>.
- [12] I.E. Idelchik, “Flow through Orifices with Change in Velocity and Flow Area.” Handbook of Hydraulic resistance. Redding: Begell House, Inc., 2007. pg255. Print.
- [13] J.P. Oosterhuis, S. Bühler, D. Wilcox, T.H. van der Meer, “Computational Fluid Dynamics Analysis of the Oscillatory Flow in a Jet Pump: The Influence of Taper Angle”. 9th PAMIR International Conference, 2014.

- [14] M. Born and E. Wolf, “Principles of optics: electromagnetic theory of propagation, interference and diffraction of light”. Fifth. Oxford [etc.]: Pergamon Press, 1975.
- [15] M. Iguchi, M. Ohmi, and K. Maegawa, “Analysis of free oscillating flow in a U-shaped tube”. Bull. JSME 25, 13981405 (1982).
- [16] P.C.H. Aben, “High-Amplitude Thermoacoustic Flow Interacting with Solid Boundaries”. Technical University of Eindhoven, 2010.
- [17] P.H.M.W in 't Panhuis. “Mathematical Aspects of Thermoacoustics”. Phd thesis, Technische Universiteit Eindhoven, 2009.
- [18] S. Backhaus and G.W. Swift, “A thermoacoustic-Stirling heat engine: Detailed study”. Condensed Matter and Thermal Physics Group, Los Alamos National Laboratory, New Mexico, 16 February 2000.
- [19] S. Backhaus and G.W. Swift, “New Varieties of Thermoacoustic Engines”. Condensed Matter and Thermal Physics Group, Los Alamos, International Congress on Sound and Vibration, July 2002.
- [20] S. Lamboo, “Setup Design for Flow Visualization of Oscillating Flow”. Thermal Engineering, University of Twente, Enschede, August 2013.
- [21] U. Ingård and S. Labate, “Acoustic Circulation Effects and the Nonlinear Impedance of Orifices”. Massachusetts Institute of Technology, Massachusetts, 1949.

# 8 Appendix

## 8.1 Preliminary experiments

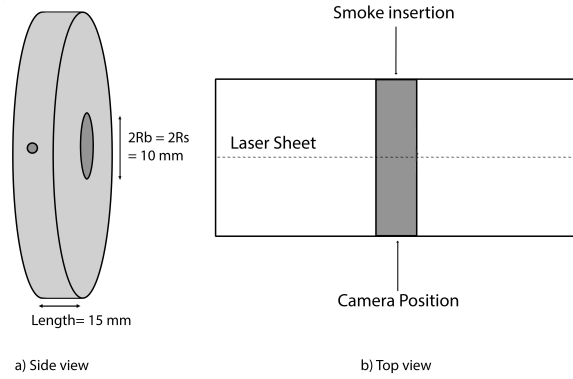


Figure 8.1: Sketch of orifice

The orifice which is placed inside the resonator tube in the existing set-up has the dimensions:  $R_b = 5 \text{ mm}$ ,  $R_s = 5 \text{ mm}$ ,  $R_{curv} = 0 \text{ mm}$ , and a length of 15 mm, as seen in sketch a) in Figure 8.1. Based on previous research [20] for the preliminary experiments the smoke is inserted perpendicular to the flow, 90 degrees with respect to the laser sheet (opposite to the camera), seen in Figure 8.1b. The smoke machine is set such that sufficient smoke flows into the set-up, which occurs around 9 V. All experiments are performed at 100Hz due to the relevance of this frequency for further thermoacoustic research. The goal of the preliminary experimentation is to determine how low the audio volume can be tuned while still leading measurable pressure that is not dominated by noise. The audio volume is set at 0.27 V and varied to observe the mean pressure in the set-up. At a voltage of 0.35 V a mean pressure of 20 Pa was distinguished without too much noise and various flow patterns were observed. With the camera set at a shutter speed of 1/1000, an aperture of F3.3 and an ISO value of 12,800 the following photographs were taken of the flow patterns, see Figure 8.2 and Figure 8.3. Figure 8.2 shows the flow as the smoke is initially entering the set-up, indicating the lighting and velocity of the flow in the jet pump is sufficient to take a representative photo. In Figure 8.3 a hole towards the end of the set-up was opened which allows air to pass from the tube to the surroundings, causing a greater burst of flow due to the sudden change in pressure in the tube. This illustrates a problem in the set-up which needs to be addressed, as the build up of smoke in the tube leads to unclear pictures, yet the sudden release of smoke leads to inaccuracies in the flow patterns and pressure drop.

From Figure 8.2 and Figure 8.3 it can be concluded that the settings used in the preliminary experiments lead to a maximum flow velocity in the jet pump at which photographs can be made. The maximum flow velocity is found by rewriting Equation (3.16) to the form shown in Equation (8.1), both equations only being valid for traveling waves. Although this equation is defined for the jet pump, it is also applicable for the orifice which was used in the set-up. The most important difference is that the  $R_b$  and  $R_s$  are equal in size for the orifice, however, this does not influence the formula. Using the geometry of the orifice,  $R_s = R_b = 5 \text{ mm}$  at a far field pressure of  $|P_I|_{FF} = 20 \text{ Pa}$  this results in a velocity in the orifice of  $|u_I|_{JP} = 1.8 \text{ m/s}$ .



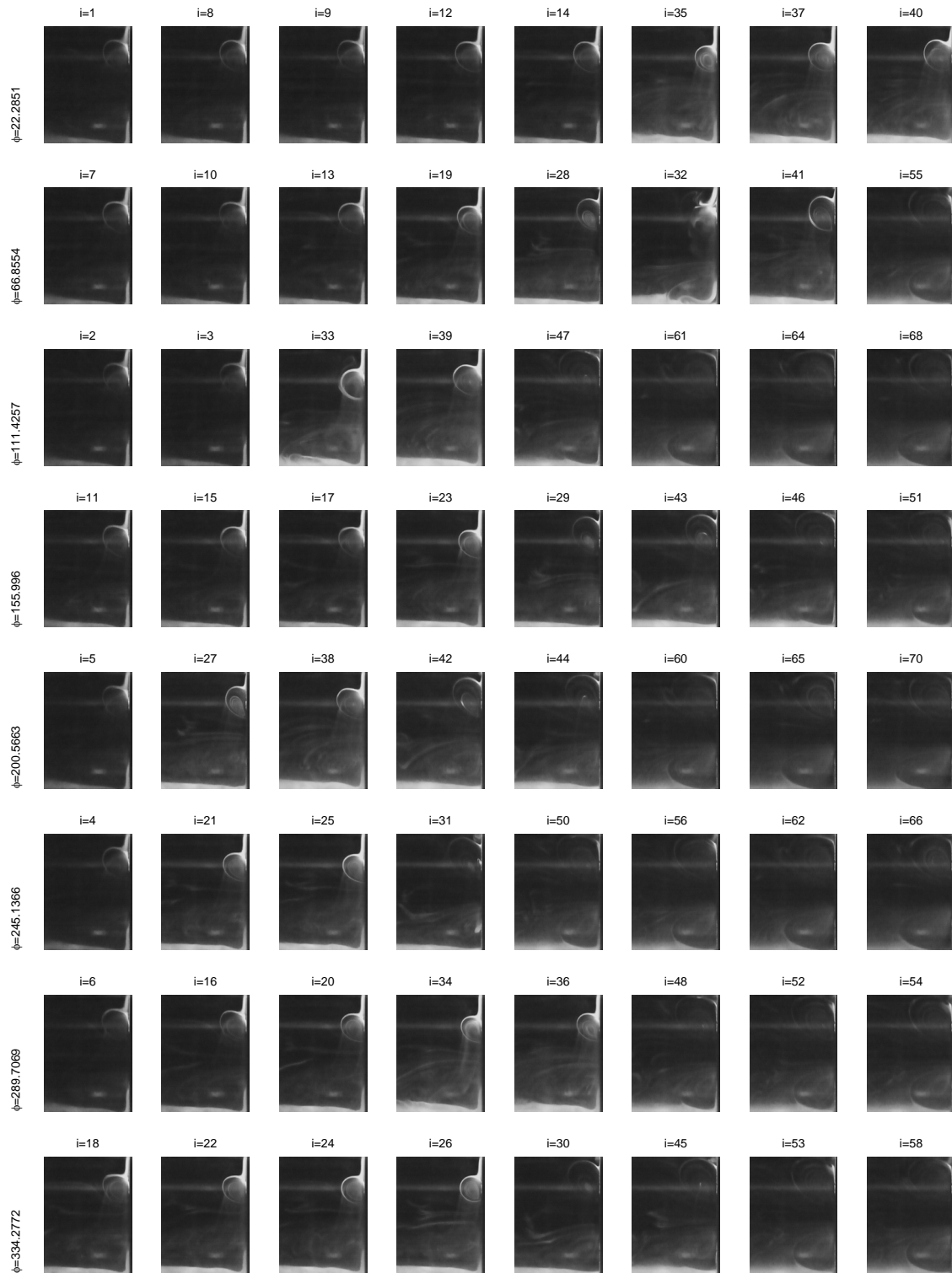
Figure 8.2: Flow visualization with shutter speed 1/1000 sec, F/3.2 and ISO 25,600



Figure 8.3: Flow visualization at with shutter speed 1/1000 sec, F/3.2 and ISO 25,600 with tube open

$$|u_I|_{JP} = \frac{R_0^2}{R_s^2} \frac{|P_I|_{FF}}{\rho_0 c_0} \quad (8.1)$$

## 8.2 Flow studied per phase at a pressure amplitude of 40 Pa, 60 Pa and 80 Pa







### 8.3 Flow studied per phase at a pressure amplitude of 60 Pa with the smoke injected before the jet pump

